

# Potential effects of the marine carbon cycle on the multiple equilibria window of the Atlantic Meridional Overturning Circulation

Amber Boot<sup>1</sup>, Anna S. von der Heydt<sup>2</sup>, and Henk A. Dijkstra<sup>3</sup>

<sup>1</sup>Institute for Marine and Atmospheric Research Utrecht

<sup>2</sup>Institute for Marine and Atmospheric research Utrecht, Utrecht University

<sup>3</sup>Institute for Marine and Atmospheric research Utrecht

September 26, 2023

## Abstract

The Atlantic Meridional Overturning Circulation (AMOC) is considered to be a tipping element in the Earth System with multiple stable states. Here, we investigate the multiple equilibria window of the AMOC within a coupled ocean circulation-carbon cycle box model. We show that adding couplings between the ocean circulation and the carbon cycle model affects the multiple equilibria window of the AMOC. Increasing the total carbon content of the system will widen the multiple equilibria window of the AMOC, since higher atmospheric pCO<sub>2</sub> values are accompanied by stronger freshwater forcing over the Atlantic ocean which acts to increase the window. Our results suggest that future changes in the marine carbon cycle can influence AMOC stability in future climates.



## Abstract

The Atlantic Meridional Overturning Circulation (AMOC) is considered to be a tipping element in the Earth System with multiple stable states. Here, we investigate the multiple equilibria window of the AMOC within a coupled ocean circulation-carbon cycle box model. We show that adding couplings between the ocean circulation and the carbon cycle model affects the multiple equilibria window of the AMOC. Increasing the total carbon content of the system will widen the multiple equilibria window of the AMOC, since higher atmospheric  $p\text{CO}_2$  values are accompanied by stronger freshwater forcing over the Atlantic ocean which acts to increase the window. Our results suggest that future changes in the marine carbon cycle can influence AMOC stability in future climates.

## Plain Language Summary

The Atlantic Meridional Overturning Circulation (AMOC), an important circulation system in the Earth System, is considered to be a tipping element with multiple stable states. In this study we investigate the range in which these multiple stable states exist, termed the multiple equilibria window, with a simple coupled ocean circulation-carbon cycle box model. We show that depending on the coupling between the ocean circulation model and the carbon cycle model, the multiple equilibria window of the AMOC changes, where it can become both smaller and larger. Furthermore, we also show that when total carbon content in the ocean-atmosphere system is increased, the width of the multiple equilibria window is increased. These results suggest that the marine carbon cycle has influenced AMOC stability in past climates, and can influence it in future climates.

## 1 Introduction

The Atlantic Meridional Overturning Circulation (AMOC) transports heat from the Southern to the Northern Hemisphere and thereby plays a large role in modulating global climate (Vellinga & Wood, 2008; Palter, 2015). It is one of the prominent tipping elements in the Earth System (Lenton et al., 2008; McKay et al., 2022). Model studies suggest that the AMOC has multiple stable states: the on-state, representing the current AMOC state with a strong northward flow at the surface and a southward return flow at intermediate depth; and the off-state, representing a weak or even reversed AMOC state (Weijer et al., 2019). From a dynamical systems point of view, a bi-stable AMOC regime appears through the occurrence of two saddle node bifurcations (Dijkstra, 2007) and the region in parameter space where both on- and off-states co-exist is the multiple equilibria window (MEW), also referred to as the bi-stability window (Barker & Knorr, 2021).

Climate variability in the past, such as Heinrich events, has been linked to tipping of the AMOC (Rahmstorf, 2002; Lynch-Stieglitz, 2017). Under anthropogenic forcing, the global warming threshold for AMOC tipping has been recently estimated to be around  $4^\circ\text{C}$  (McKay et al., 2022). Model data from the Coupled Model Intercomparison Project 6 (CMIP6; Eyring et al., 2016), Weijer et al. (2020) project a consistent weakening of the AMOC under future climate change, with a 34-45% decrease in AMOC strength in 2100, but no clear tipping was found. However, these models may have a too stable AMOC (Weijer et al., 2019) and the probability of AMOC tipping before 2100 may still be non-negligible. Under AMOC tipping, a strong cooling in the Northern Hemisphere (Rahmstorf, 2002; Drijfhout, 2015), changes in the water cycle (Vellinga & Wood, 2002; Jackson et al., 2015), and potential interactions with other tipping elements in the Earth System (Dekker et al., 2018; Wunderling et al., 2021; Sinet et al., 2023) are expected.

The AMOC can also interact with the marine carbon cycle and therefore influence atmospheric  $p\text{CO}_2$ . By affecting the transport of important tracers, such as dissolved

inorganic carbon (DIC), total alkalinity, and nutrients, the AMOC affects the solubility and biological carbon pumps. Evidence for a coupling between the AMOC and marine carbon cycle is provided in proxy data (Bauska et al., 2021). Model studies show a wide range of potential carbon cycle responses to a collapse of the AMOC. While most models show an increase in atmospheric  $p\text{CO}_2$  (e.g. Marchal et al., 1998; Schmittner & Galbraith, 2008; Matsumoto & Yokoyama, 2013), the magnitude and precise mechanisms are dependent on the model used and climatic boundary conditions (Gottschalk et al., 2019).

As the AMOC can influence atmospheric  $p\text{CO}_2$ , there is a potential feedback mechanism since  $\text{CO}_2$  influences the hydrological cycle (Weijer et al., 2019; Barker & Knorr, 2021) and, through changes in buoyancy fluxes, affects the AMOC. Previous studies suggest that there may be a relation between atmospheric  $p\text{CO}_2$  and the MEW of the AMOC (Barker et al., 2010, 2015). However, a clear mechanistic view has not been given yet. Here, we study the mechanisms on how the marine carbon cycle affects the MEW of the AMOC using a coupled Atlantic Ocean circulation-carbon cycle box model.

## 2 Method

We couple an Atlantic Ocean circulation model (Cimatoribus et al., 2014; Castellana et al., 2019) to a carbon cycle model (O'Neill et al., 2019; Boot et al., 2022). The ocean circulation model (Fig. 1) simulates the distribution of salinity in 5 ocean boxes and the depth of the pycnocline in the Atlantic Ocean and is well suited to simulate AMOC dynamics (Cimatoribus et al., 2014). Salinity in the model is affected by wind and buoyancy driven ocean flows and by freshwater fluxes. The carbon-cycle model simulates DIC, alkalinity (Alk) and phosphate ( $\text{PO}_4$ ) and captures relevant processes such as riverine input, air-sea gas exchange, biological export production,  $\text{CaCO}_3$  rain,  $\text{CaCO}_3$  dissolution and sediment burial (Fig. 1). The AMOC influences the carbon cycle directly by advective transport of the tracers and the simulated salt distributions in the AMOC model are used as input for the carbonate chemistry and tracer transport in the carbon-cycle model. An important coupling between both models is due to the fact that biological export production is dependent on nutrient transport. By representing the symmetrical component of the freshwater forcing  $E_s$  of the AMOC model (Fig. 1) as a function of atmospheric  $p\text{CO}_2$ , another important coupling between both models is represented.

To determine the functional relation between  $p\text{CO}_2$  and  $E_s$ , we use a fit from a CMIP6 multi-model mean, based on 28 models, simulated under the 1%  $\text{CO}_2$  increase scenario (Eyring et al., 2016). We fit both a linear and logarithmic function to atmospheric  $p\text{CO}_2$  data and the freshwater flux into the ocean region represented by the thermocline box in our model (box  $t$  in Fig. 1). There is net evaporation over this region which represents  $2 E_s$  in the box model resulting in the linear (Eq. 1) and logarithmic (Eq. 2) fits shown in Figure S1. We will use both fits in section 3.1 since the fits show different behavior for  $p\text{CO}_2$  values lower than 300 ppm, and by using both we test the sensitivity of the model to the used fit. The fits (in Sv) are given by:

$$E_s = 0.562 + 0.00012 \times p\text{CO}_2 \quad (1)$$

$$E_s = 0.099 + 0.079 \times \ln(p\text{CO}_2) \quad (2)$$

Both relations above capture the effect of  $\text{CO}_2$  induced warming on the hydrological cycle that results in the subtropical regions becoming drier under higher  $p\text{CO}_2$  values, while sub-polar regions become wetter, which is indeed seen in both model and paleo proxy studies (Held & Soden, 2006; Bonfils et al., 2020; van der Ploeg et al., 2023).

The relations (Eq. 1) and (Eq. 2) could only be determined from the CMIP6 models over a limited range of  $p(\text{CO}_2)$  and only for time varying climates. To extend that

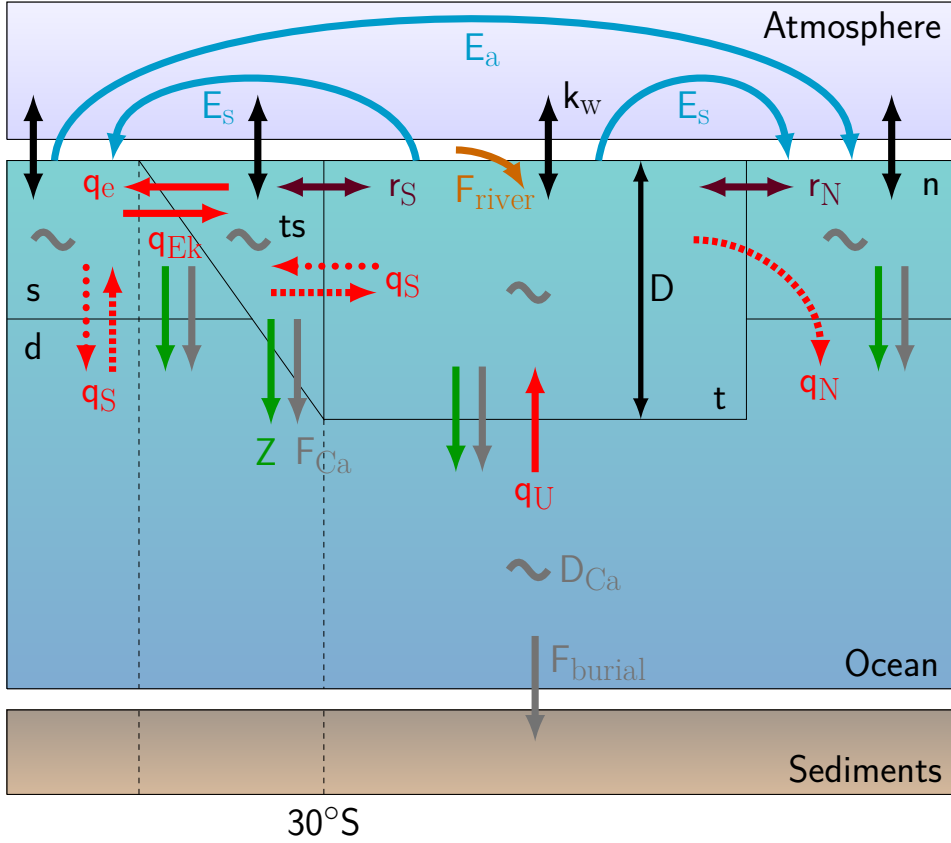


**Figure 1.** Box structure and processes simulated in the coupled circulation – carbon cycle model. Red arrows represent volume transports where dashed arrows are only present during an on-state, and dotted arrows only present during an off-state. The purple arrows represent gyre exchange ( $r_N$  and  $r_S$ ), and blue arrows freshwater fluxes ( $E_s$  for the symmetrical forcing, and  $E_a$  for the asymmetrical forcing). Carbon cycle processes that are represented are riverine input (orange), air-sea gas exchange (black;  $k_w$ ), biological export production (green;  $Z$ ),  $\text{CaCO}_3$  rain (grey;  $F_{Ca}$ ),  $\text{CaCO}_3$  dissolution (grey;  $D_{Ca}$ ), and sediment burial (grey;  $F_{burial}$ ). Based on Castellana et al. (2019) and Boot et al. (2022).

112 range and to capture the possibility that the fits (Eq.1 and 2) do not accurately repre-  
 113 sent the  $E_s$ - $p\text{CO}_2$ -coupling in steady state climates, we also use a third relation

$$E_s = 0.1 + 0.75 \times \ln\left(\frac{p\text{CO}_2 + 250}{p\text{CO}_{2,0}}\right) \quad (3)$$

114 to demonstrate the effect of the carbon cycle on the AMOC MEW for a larger range of  
 115 possible  $E_s$ - $p\text{CO}_2$  coupling strengths. The parameter values in (Eq. 3) are tuned such  
 116 that  $E_s$  approaches 0 when atmospheric  $p\text{CO}_2$  approaches 0, and that  $E_s = E_{s,base}$  (0.56 Sv)  
 117 when atmospheric  $p\text{CO}_2$  is equal to  $p\text{CO}_{2,0} = 300$  ppm. When the  $\text{CO}_2$  concentration  
 118 exceeds  $p\text{CO}_{2,0}$ ,  $E_s$  will be larger than  $E_{s,base}$ . Both logarithmic fits (Eq. 2 and Eq. 3)  
 119 are used in sections 3.1 and 3.2.

### 3 Results

The equations of the coupled model (see Supporting Information) are implemented in the continuation software AUTO-07p (Doedel et al., 2007), which is able to efficiently compute branches of steady state solutions in parameter space and to detect the saddle-node bifurcations bounding the MEW. For the AMOC bifurcation diagram, we use the asymmetric component of the freshwater flux  $E_a$  as a control parameter as in Castellana et al. (2019). In the results below, we will consider four different cases of the model related to capturing different carbon-cycle processes. In case REF we use the default coupled circulation-carbon cycle model. In BIO we add the coupling of export production to the ocean circulation. In BIO+ $E_s$ , the  $E_s$ -pCO<sub>2</sub> coupling is added, and lastly, in case BIO+ $E_s$ +FCA, the rain ratio is modelled as a function of the calcium carbonate (CaCO<sub>3</sub>) saturation state, whereas in the other three cases it is constant (see also Table S1 for the specifics of the different cases).

#### 3.1 The AMOC multiple equilibria window

The bifurcation diagrams, showing the AMOC strength versus  $E_a$  are for the three  $E_s$ -pCO<sub>2</sub> relations (Eq. 1), (Eq. 2) and (Eq. 3) in Fig. 2a-b, Fig. 2c-d and Fig. 2e-f, respectively.

To be able to simulate both the on- and off-branch in the coupled model, it is vital that the BIO coupling is used, since otherwise phosphate concentration in the surface ocean will become negative under a collapsed AMOC regime. This behavior is illustrated in Fig. 2a, b by the cases REF and BIO. In case REF the off-branch is not shown, while for case BIO the full bifurcation diagram with two saddle-node bifurcations is plotted. Atmospheric pCO<sub>2</sub> also shows hysteresis behavior with low concentrations on the off-branch (around 50 ppm).

To explain the low pCO<sub>2</sub> values on- the off-branch we look at the constraint in the model on total carbon content in the ocean-atmosphere system. In steady state, the riverine input and sediment outflux of DIC must balance to keep the total carbon content constant (in time). In our model, the sediment outflux is a function of the saturation state of CaCO<sub>3</sub> and CaCO<sub>3</sub> flux which is a function of the rain ratio (constant in non-FCA cases) and the export production. However, in this model set up, the saturation state of CaCO<sub>3</sub> in the ocean is in every box larger than 1, meaning that there is no saturation driven dissolution of CaCO<sub>3</sub> and the sediment outflux is purely a function of the export production. In an AMOC off-state, nutrient advection is low causing a large reduction in export production, and therefore a small sediment outflux. The riverine influx must balance this small outflux, which can only be achieved by decreasing atmospheric pCO<sub>2</sub> to the values reported on the off-branch. When the rain ratio feedback is used (case FCA), this mechanism is also present, but the sediment outflux is in this case also a function of the rain ratio. In the FCA case, the rain ratio is variable when the saturation state of CaCO<sub>3</sub> is larger than 1. This results in larger rain ratio values, and therefore more CaCO<sub>3</sub> export to the sediments increasing the sediment outflux and, through the river influx, atmospheric pCO<sub>2</sub>.

When the linear CMIP6  $E_s$ -pCO<sub>2</sub> coupling (Eq. 1) is used, the MEW increases slightly. The saddle node on the on-branch shifts from 0.45Sv to 0.46Sv, and the saddle node on the off-branch shifts from -0.08Sv to -0.10Sv for both  $E_s$ +BIO and  $E_s$ +BIO+FCA. Due to the presence of a subcritical Hopf bifurcation in the AMOC model, the on-branch becomes unstable before the saddle node. The presence of the Hopf bifurcation is not further considered in this study as we are only interested in the MEW. The small movement of the saddle nodes in parameter space shows that when the linear CMIP6 fit is used, the CO<sub>2</sub> dependency of  $E_s$  is too weak to significantly impact the MEW. When the logarithmic CMIP6 fit (Eq. 2) is used, the MEW becomes smaller (Fig. 2c, d). The logarithmic fit (Eq. 3) over the full pCO<sub>2</sub> range shows that the marine carbon cycle can

171 have a substantial effect on the AMOC MEW, as the saddle node on the off-branch moves  
172 to larger values of  $E_a$ .

173 To explain the movement of the saddle nodes, we consider the sensitivity of the model  
174 to  $E_s$  (Figure S1). The default value used for cases REF and BIO for  $E_s$  is 0.56 Sv. The  
175 logarithmic CMIP6 fit results in a slightly smaller value, whereas the linear fit has a slightly  
176 larger value. Due to increased  $E_s$ , the thermocline becomes saltier, and in combination  
177 with the salt-advection feedback, this leads to a larger meridional density gradient and  
178 therefore a stronger AMOC. Furthermore, increased  $E_s$  increases the net evaporation over  
179 the Atlantic, given by  $(E_s - E_a)$  and a larger  $E_a$  is necessary to tip the AMOC. On the  
180 off-branch, a larger  $E_s$  results in salinification of the  $ts$  box and a more negative fresh-  
181 water flux ( $E_a$ ) is needed to increase the meridional density gradient and reinvigorate  
182 the AMOC. This behavior of the AMOC model explains the differences between Figs.  
183 2a-b and 2c-d. The fit Eq. 3 narrows the MEW by moving the saddle node on the off-  
184 branch to larger values of  $E_a$  (Fig. 2e, f). Using this fit shows more clearly that there  
185 can be an influence on the MEW via a coupling to atmospheric  $p\text{CO}_2$ . Here, it reduces  
186 the MEW by moving the off-branch saddle node to larger values of  $E_a$  which can be ex-  
187 plained by the fact that  $\text{CO}_2$  on the off-branch is smaller than  $\text{CO}_{2,0}$  and therefore  $E_s$   
188 is smaller than  $E_{s,base}$ .

### 189 3.2 Sensitivity to total carbon content

190 Over the Cenozoic, both the AMOC (Lynch-Stieglitz, 2017) and total carbon con-  
191 tent in the ocean-atmosphere system have varied (Zeebe et al., 2009; Caves et al., 2016).  
192 In Caves et al. (2016) it is suggested that total carbon content has varied between 24,000  
193 PgC and 96,000 PgC. In the previous section, the model was studied with approximately  
194 8000 PgC in the Atlantic and Southern Ocean which translates to approximately 40,000  
195 PgC in the global system (since our model represents approximately 20% of the global  
196 ocean). In this section, we analyze how the sensitivity to  $E_a$  changes under different to-  
197 tal carbon contents in the model. To test the sensitivity, we remove approximately 2000  
198 (-25%) PgC, and add approximately 2000 (+25%), 4000 (+50%) and 8000 (+100%) PgC.  
199 We do this for the CMIP6 logarithmic coupling (Eq. 2; Fig. 3a-c) and the strong log-  
200 arithmic coupling (Eq. 3; Fig. 3d-f). Both cases show similar results, but in Fig. 3a-c  
201 the MEW changes are less pronounced; we therefore focus on the results in Fig. 3d-f.

202 The MEW increases when total carbon increases. There is, however, a different re-  
203 sponse when the rain ratio feedback (FCA) is included. For case  $E_s$ +BIO we see that  
204 the MEW increases under a total C change from -2000 PgC to +2000 PgC, but then re-  
205 mains constant for more carbon content. We can explain this by looking at the atmo-  
206 spheric  $p\text{CO}_2$  values, and therefore also  $E_s$ , at the saddle node, which are similar for the  
207 three high carbon cases. When the rain ratio feedback is used, we see that the MEW keeps  
208 increasing for larger carbon contents since also the atmospheric  $p\text{CO}_2$  increases. We can  
209 explain the difference between  $E_s$ +BIO and  $E_s$ +BIO+FCA by the constraint on total  
210 carbon in the ocean-atmosphere system. In  $E_s$ +BIO, biological export production is mainly  
211 a function of the AMOC strength, whereas in the  $E_s$ +BIO+FCA case it is also depen-  
212 dent on the  $\text{CaCO}_3$  saturation state which is coupled to atmospheric  $p\text{CO}_2$  through the  
213 pH of the surface ocean. This increases the biological export production, and through  
214 the same mechanisms as described before, higher atmospheric  $p\text{CO}_2$  values.

## 215 4 Summary and discussion

216 In this paper we investigated the multiple equilibria window (MEW) of the AMOC  
217 in a coupled ocean circulation-carbon cycle box model. When freshwater forcing is cou-  
218 pled to atmospheric  $p\text{CO}_2$  using CMIP6 multi-model fits (Eq. 1 and Eq. 2), the MEW  
219 changes slightly due to a weak dependency on atmospheric  $p\text{CO}_2$ . However, when we  
220 use a stronger coupling (Eq. 3), the saddle node on the off-branch moves towards larger

221  $E_a$  values and thereby reduces the MEW. We also assessed the sensitivity to total car-  
222 bon content in the system and found that the MEW is larger with more carbon in the  
223 system due to a shift of both the on- and off-branch saddle nodes. Both results show the  
224 potential of the marine carbon cycle to influence the MEW of the AMOC.

225 We acknowledge that it is difficult to provide an adequate justification of the dif-  
226 ferent  $E_s$ - $p\text{CO}_2$  relations because the CMIP6 model  $p\text{CO}_2$  range is too small and there  
227 are no observations which can test the strong coupling relation (Eq. 3). However, from  
228 the results clear and plausible mechanisms can be extracted which cause the change in  
229 MEW and these are more important than the precise quantitative estimates. Two pro-  
230 cesses explain the results on the MEW: (1) the balance between the river flux and sed-  
231 iment flux that constrains atmospheric  $p\text{CO}_2$ ; and (2) the sensitivity of the AMOC to  
232  $E_s$ . In the model, atmospheric  $p\text{CO}_2$  is dependent on the ocean circulation through ex-  
233 port production,  $E_s$  is dependent on atmospheric  $p\text{CO}_2$ , and the ocean circulation is de-  
234 pendent on  $E_s$ , creating a feedback loop (Fig. 4). We see that when atmospheric  $p\text{CO}_2$   
235 is high, so is  $E_s$  which results in a stronger AMOC on the on-branch. As a consequence,  
236 export production is increased and there will be a larger outflux of carbon and alkalin-  
237 ity through the sediments, which is balanced by a high influx of carbon through the rivers,  
238 consistent with high atmospheric  $p\text{CO}_2$  values. Of the feedbacks that we have implemented,  
239 only the rain ratio feedback (FCA) affects this mechanism because it directly influences  
240 the sediment outflux and makes the carbon cycle less sensitive to the ocean circulation.  
241

242 The results here can be relevant when studying climate transitions in past and fu-  
243 ture climates as it identifies mechanisms how AMOC stability can depend on background  
244 climate and atmospheric  $p\text{CO}_2$  values. Previous work focused on the Pleistocene sug-  
245 gest an influence of atmospheric  $p\text{CO}_2$  on the stability structure of the AMOC through  
246 temperature (Sun et al., 2022) and moisture transport (Zhang et al., 2017). In our model,  
247 there is no effect of temperature changes, but the  $E_s$  coupling used here is similar to the  
248 moisture transport described in Zhang et al. (2017) the only difference being that this  
249 moisture transport is to the Pacific basin, whereas in our model it is redistributed over  
250 the Atlantic to conserve salinity.

251 We have used a model that provides a simple framework for studying AMOC dy-  
252 namics that allows us to efficiently test the concept of AMOC stability in a wide range  
253 of parameter values. However, a limitation is that the model only represents a fifth of  
254 the global ocean, the Atlantic and Southern Ocean. For the circulation model this might  
255 not be a large deficiency, but for the carbon cycle model it might be. Furthermore, the  
256 coupled model might not be valid for the entire parameter space we have simulated. An  
257 example of this, is the unrealistic low  $p\text{CO}_2$  values on the off-branch. These low values  
258 suggest that some important processes are missing, e.g. negative feedbacks arising in the  
259 Indo-Pacific basin or in the terrestrial biosphere. Though not a limitation in the model,  
260 it is good to note that the range of timescales in the carbon cycle model is larger than  
261 in the circulation model, which does not affect our results but does affect the time de-  
262 pendent response of the system.

263 Our work also holds implications for assessing AMOC stability in future climates.  
264 Currently, the global warming threshold for an AMOC collapse is estimated to be 4 °C  
265 (McKay et al., 2022). In the future, the carbon content of the ocean-atmosphere system  
266 will increase, potentially increasing the MEW which can change the likelihood of a bi-  
267 furcation induced AMOC collapse. In this study we focused on slow, bifurcation induced  
268 tipping of the AMOC, while the AMOC is also able to tip due to faster processes result-  
269 ing in noise-induced tipping (Castellana et al., 2019). We hope this work inspires fur-  
270 ther research on the dependency of the MEW of the AMOC on the carbon cycle in more  
271 detailed models to further investigate the relevance of the mechanism found in this study  
272 and provide a quantification for the influence of the marine carbon cycle on the MEW  
273 of the AMOC.

274 **Appendix A Open Science**

275 Model code, generated model data, scripts for plotting all figures can be found at  
 276 10.5281/zenodo.8042693 (Boot et al., 2023). A list of used datasets, processed datasets  
 277 and citations for the CMIP6 multi-model fits is also included in this repository. CMIP6  
 278 model data can be downloaded from the Earth System Grid Federation (ESGF) ([https://  
 279 esgf-node.llnl.gov/search/cmip6/](https://esgf-node.llnl.gov/search/cmip6/)). AUTO-07p can be downloaded from [https://  
 280 github.com/auto-07p](https://github.com/auto-07p).

281 **Acknowledgments**

282 This study has been supported by the Netherlands Earth System Science Centre (NESSC),  
 283 which is financially supported by the Ministry of Education, Culture and Science (OCW;  
 284 grant no. 024.002.001)

285 **References**

- 286 Andersson, A., Graw, K., Schröder, M., Fennig, K., Liman, J., Bakan, S., ... Klepp,  
 287 C. (2017). *Hamburg Ocean Atmosphere Parameters and Fluxes from Satel-  
 288 lite Data - HOAPS 4.0*. Satellite Application Facility on Climate Monitor-  
 289 ing (CM SAF). Retrieved from [https://wui.cmsaf.eu/safira/action/  
 290 viewDoiDetails?acronym=HOAPS{\\\_}V002](https://wui.cmsaf.eu/safira/action/viewDoiDetails?acronym=HOAPS{\_}V002) doi: 10.5676/EUM.SAF\_CM/  
 291 HOAPS/V002
- 292 Barker, S., Chen, J., Gong, X., Jonkers, L., Knorr, G., & Thornalley, D. (2015). Ice-  
 293 bergs not the trigger for North Atlantic cold events. *Nature*, *520*(7547), 333–  
 294 336. Retrieved from <https://doi.org/10.1038/nature14330> doi: 10.1038/  
 295 nature14330
- 296 Barker, S., & Knorr, G. (2021). Millennial scale feedbacks determine the shape and  
 297 rapidity of glacial termination. *Nature Communications*, *12*(1), 2273. Re-  
 298 trieved from <https://doi.org/10.1038/s41467-021-22388-6> doi: 10.1038/  
 299 s41467-021-22388-6
- 300 Barker, S., Knorr, G., Vautravers, M. J., Diz, P., & Skinner, L. C. (2010). Extreme  
 301 deepening of the Atlantic overturning circulation during deglaciation. *Na-  
 302 ture Geoscience*, *3*(8), 567–571. Retrieved from [https://doi.org/10.1038/  
 303 ngeo921](https://doi.org/10.1038/ngeo921) doi: 10.1038/ngeo921
- 304 Bauska, T. K., Marcott, S. A., & Brook, E. J. (2021). Abrupt changes in the global  
 305 carbon cycle during the last glacial period. *Nature Geoscience*, *14*(2), 91–  
 306 96. Retrieved from <https://doi.org/10.1038/s41561-020-00680-2> doi:  
 307 10.1038/s41561-020-00680-2
- 308 Bonfils, C. J. W., Santer, B. D., Fyfe, J. C., Marvel, K., Phillips, T. J., & Zim-  
 309 merman, S. R. H. (2020). Human influence on joint changes in tempera-  
 310 ture, rainfall and continental aridity. *Nature Climate Change*, *10*(8), 726–  
 311 731. Retrieved from <https://doi.org/10.1038/s41558-020-0821-1> doi:  
 312 10.1038/s41558-020-0821-1
- 313 Boot, A., von der Heydt, A. S., & Dijkstra, H. A. (2022). Effect of the At-  
 314 lantic Meridional Overturning Circulation on atmospheric  $\text{CO}_2$   
 315 variations. *Earth System Dynamics*, *13*(3), 1041–1058. Retrieved from  
 316 <https://esd.copernicus.org/articles/13/1041/2022/> doi: 10.5194/  
 317 esd-13-1041-2022
- 318 Boot, A., von der Heydt, A. S., & Dijkstra, H. A. (2023, June). *AMOC MEW GRL*.  
 319 [dataset]. Zenodo. doi: 10.5281/zenodo.8042693
- 320 Castellana, D., Baars, S., Wubs, F. W., & Dijkstra, H. A. (2019). Transition Prob-  
 321 abilities of Noise-induced Transitions of the Atlantic Ocean Circulation. *Scien-  
 322 tific Reports*, *9*(1), 20284. Retrieved from [https://doi.org/10.1038/s41598-  
 323 -019-56435-6](https://doi.org/10.1038/s41598-019-56435-6) doi: 10.1038/s41598-019-56435-6
- 324 Caves, J. K., Jost, A. B., Lau, K. V., & Maher, K. (2016). Cenozoic carbon cycle

- 325 imbalances and a variable weathering feedback. *Earth and Planetary Science*  
 326 *Letters*, *450*, 152–163. Retrieved from [https://www.sciencedirect.com/](https://www.sciencedirect.com/science/article/pii/S0012821X16303223)  
 327 [science/article/pii/S0012821X16303223](https://www.sciencedirect.com/science/article/pii/S0012821X16303223) doi: [https://doi.org/10.1016/](https://doi.org/10.1016/j.epsl.2016.06.035)  
 328 [j.epsl.2016.06.035](https://doi.org/10.1016/j.epsl.2016.06.035)
- 329 Cimadoribus, A. A., Drijfhout, S. S., & Dijkstra, H. A. (2014). Meridional overturn-  
 330 ing circulation: stability and ocean feedbacks in a box model. *Climate Dynam-*  
 331 *ics*, *42*(1), 311–328. Retrieved from [https://doi.org/10.1007/s00382-012-](https://doi.org/10.1007/s00382-012-1576-9)  
 332 [1576-9](https://doi.org/10.1007/s00382-012-1576-9) doi: 10.1007/s00382-012-1576-9
- 333 Dekker, M. M., von der Heydt, A. S., & Dijkstra, H. A. (2018). Cascading transi-  
 334 tions in the climate system. *Earth System Dynamics*, *9*(4), 1243–1260. Re-  
 335 trieved from <https://esd.copernicus.org/articles/9/1243/2018/> doi: 10  
 336 .5194/esd-9-1243-2018
- 337 Dijkstra, H. A. (2007, oct). Characterization of the multiple equilibria regime in  
 338 a global ocean model. *Tellus A*, *59*(5), 695–705. Retrieved from [https://](https://doi.org/10.1111/j.1600-0870.2007.00267.x)  
 339 [doi.org/10.1111/j.1600-0870.2007.00267.x](https://doi.org/10.1111/j.1600-0870.2007.00267.x) doi: [https://doi.org/10.1111/](https://doi.org/10.1111/j.1600-0870.2007.00267.x)  
 340 [j.1600-0870.2007.00267.x](https://doi.org/10.1111/j.1600-0870.2007.00267.x)
- 341 Doedel, E. J., Paffenroth, R. C., Champneys, A. C., Fairgrieve, T. F., Kuznetsov,  
 342 Y. A., Oldeman, B. E., ... Wang, X. J. (2007). *AUTO-07p: Continuation and*  
 343 *Bifurcation Software for Ordinary Differential Equations*.
- 344 Drijfhout, S. (2015). Competition between global warming and an abrupt collapse of  
 345 the AMOC in Earth’s energy imbalance. *Scientific Reports*, *5*(1), 14877. Re-  
 346 trieved from <https://doi.org/10.1038/srep14877> doi: 10.1038/srep14877
- 347 Eyring, V., Bony, S., Meehl, G. A., Senior, C. A., Stevens, B., Stouffer, R. J., &  
 348 Taylor, K. E. (2016, may). Overview of the Coupled Model Intercompari-  
 349 son Project Phase 6 (CMIP6) experimental design and organization. *Geosci.*  
 350 *Model Dev.*, *9*(5), 1937–1958. Retrieved from [https://gmd.copernicus.org/](https://gmd.copernicus.org/articles/9/1937/2016/https://gmd.copernicus.org/articles/9/1937/2016/gmd-9-1937-2016.pdf)  
 351 [articles/9/1937/2016/https://gmd.copernicus.org/articles/9/1937/](https://gmd.copernicus.org/articles/9/1937/2016/https://gmd.copernicus.org/articles/9/1937/2016/gmd-9-1937-2016.pdf)  
 352 [2016/gmd-9-1937-2016.pdf](https://gmd.copernicus.org/articles/9/1937/2016/gmd-9-1937-2016.pdf) doi: 10.5194/gmd-9-1937-2016
- 353 Follows, M. J., Ito, T., & Dutkiewicz, S. (2006). On the solution of the carbonate  
 354 chemistry system in ocean biogeochemistry models. *Ocean Modelling*, *12*(3),  
 355 290–301. Retrieved from [http://www.sciencedirect.com/science/article/](http://www.sciencedirect.com/science/article/pii/S1463500305000533)  
 356 [pii/S1463500305000533](http://www.sciencedirect.com/science/article/pii/S1463500305000533) doi: <https://doi.org/10.1016/j.ocemod.2005.05.004>
- 357 Gottschalk, J., Battaglia, G., Fischer, H., Frölicher, T. L., Jaccard, S. L., Jeltsch-  
 358 Thömmes, A., ... Stocker, T. F. (2019). Mechanisms of millennial-scale  
 359 atmospheric CO<sub>2</sub> change in numerical model simulations. *Quaternary Sci-*  
 360 *ence Reviews*, *220*, 30–74. Retrieved from [http://www.sciencedirect.com/](http://www.sciencedirect.com/science/article/pii/S0277379118310473)  
 361 [science/article/pii/S0277379118310473](http://www.sciencedirect.com/science/article/pii/S0277379118310473) doi: [https://doi.org/10.1016/](https://doi.org/10.1016/j.quascirev.2019.05.013)  
 362 [j.quascirev.2019.05.013](https://doi.org/10.1016/j.quascirev.2019.05.013)
- 363 Held, I. M., & Soden, B. J. (2006). Robust Responses of the Hydrological Cy-  
 364 cle to Global Warming. *Journal of Climate*, *19*(21), 5686–5699. Re-  
 365 trieved from [https://journals.ametsoc.org/view/journals/clim/19/](https://journals.ametsoc.org/view/journals/clim/19/21/jcli3990.1.xml)  
 366 [21/jcli3990.1.xml](https://journals.ametsoc.org/view/journals/clim/19/21/jcli3990.1.xml) doi: 10.1175/JCLI3990.1
- 367 Jackson, L. C., Kahana, R., Graham, T., Ringer, M. A., Woollings, T., Mecking,  
 368 J. V., & Wood, R. A. (2015). Global and European climate impacts of a slow-  
 369 down of the AMOC in a high resolution GCM. *Climate Dynamics*, *45*(11),  
 370 3299–3316. Retrieved from <https://doi.org/10.1007/s00382-015-2540-2>  
 371 doi: 10.1007/s00382-015-2540-2
- 372 Lenton, T. M., Held, H., Kriegler, E., Hall, J. W., Lucht, W., Rahmstorf, S., &  
 373 Schellnhuber, H. J. (2008). Tipping elements in the Earth’s climate system.  
 374 *Proceedings of the National Academy of Sciences*, *105*(6), 1786–1793. Re-  
 375 trieved from <https://www.pnas.org/doi/abs/10.1073/pnas.0705414105>  
 376 doi: 10.1073/pnas.0705414105
- 377 Lueker, T. J., Dickson, A. G., & Keeling, C. D. (2000). Ocean pCO<sub>2</sub> calculated  
 378 from dissolved inorganic carbon, alkalinity, and equations for K<sub>1</sub> and K<sub>2</sub>:  
 379 validation based on laboratory measurements of CO<sub>2</sub> in gas and seawater at

- 380 equilibrium. *Marine Chemistry*, 70(1), 105–119. Retrieved from [https://](https://www.sciencedirect.com/science/article/pii/S0304420300000220)  
 381 [www.sciencedirect.com/science/article/pii/S0304420300000220](https://www.sciencedirect.com/science/article/pii/S0304420300000220) doi:  
 382 [https://doi.org/10.1016/S0304-4203\(00\)00022-0](https://doi.org/10.1016/S0304-4203(00)00022-0)
- 383 Lynch-Stieglitz, J. (2017). The Atlantic Meridional Overturning Circulation and  
 384 Abrupt Climate Change. *Annual Review of Marine Science*, 9(1), 83–104.  
 385 Retrieved from <https://doi.org/10.1146/annurev-marine-010816-060415>  
 386 doi: 10.1146/annurev-marine-010816-060415
- 387 Marchal, O., Stocker, T. F., & Joos, F. (1998, jun). Impact of oceanic reorganiza-  
 388 tions on the ocean carbon cycle and atmospheric carbon dioxide content. *Pa-*  
 389 *leoceanography*, 13(3), 225–244. Retrieved from [https://doi.org/10.1029/](https://doi.org/10.1029/98PA00726)  
 390 [98PA00726](https://doi.org/10.1029/98PA00726) doi: <https://doi.org/10.1029/98PA00726>
- 391 Matsumoto, K., & Yokoyama, Y. (2013, jun). Atmospheric  $\Delta^{14}\text{C}$  reduction in  
 392 simulations of Atlantic overturning circulation shutdown. *Global Biogeochem-*  
 393 *ical Cycles*, 27(2), 296–304. Retrieved from [https://doi.org/10.1002/](https://doi.org/10.1002/gbc.20035)  
 394 [gbc.20035](https://doi.org/10.1002/gbc.20035) doi: <https://doi.org/10.1002/gbc.20035>
- 395 McKay, D. I. A., Staal, A., Abrams, J. F., Winkelmann, R., Sakschewski, B., Lo-  
 396 riani, S., ... Lenton, T. M. (2022). Exceeding 1.5°C global warm-  
 397 ing could trigger multiple climate tipping points. *Science*, 377(6611),  
 398 eabn7950. Retrieved from [https://www.science.org/doi/abs/10.1126/](https://www.science.org/doi/abs/10.1126/science.abn7950)  
 399 [science.abn7950](https://www.science.org/doi/abs/10.1126/science.abn7950) doi: 10.1126/science.abn7950
- 400 Millero, F. J. (1983). CHAPTER 43 - Influence of Pressure on Chemical Pro-  
 401 cesses in the Sea. In J. P. RILEY & R. B. T. C. O. CHESTER (Eds.), (pp.  
 402 1–88). Academic Press. Retrieved from [https://www.sciencedirect.com/](https://www.sciencedirect.com/science/article/pii/B9780125886086500079)  
 403 [science/article/pii/B9780125886086500079](https://www.sciencedirect.com/science/article/pii/B9780125886086500079) doi: [https://doi.org/10.1016/](https://doi.org/10.1016/B978-0-12-588608-6.50007-9)  
 404 [B978-0-12-588608-6.50007-9](https://doi.org/10.1016/B978-0-12-588608-6.50007-9)
- 405 Mucci, A. (1983, sep). The solubility of calcite and aragonite in seawater at various  
 406 salinities, temperatures, and one atmosphere total pressure. *American Journal*  
 407 *of Science*, 283, 780–799. Retrieved from [https://ui.adsabs.harvard.edu/](https://ui.adsabs.harvard.edu/abs/1983AmJS..283..780M)  
 408 [abs/1983AmJS..283..780M](https://ui.adsabs.harvard.edu/abs/1983AmJS..283..780M) doi: 10.2475/ajs.283.7.780
- 409 Munhoven, G. (2013). Mathematics of the total alkalinity–pH equation - path-  
 410 way to robust and universal solution algorithms: the SolveSAPHE pack-  
 411 age v1.0.1. *Geoscientific Model Development*, 6(4), 1367–1388. Retrieved  
 412 from <https://gmd.copernicus.org/articles/6/1367/2013/> doi:  
 413 [10.5194/gmd-6-1367-2013](https://doi.org/10.5194/gmd-6-1367-2013)
- 414 O'Neill, C. M., Hogg, A. M., Ellwood, M. J., Eggins, S. M., & Opdyke, B. N. (2019).  
 415 The [simple carbon project] model v1.0. *Geoscientific Model Development*,  
 416 12(4), 1541–1572. Retrieved from [https://gmd.copernicus.org/articles/](https://gmd.copernicus.org/articles/12/1541/2019/)  
 417 [12/1541/2019/](https://gmd.copernicus.org/articles/12/1541/2019/) doi: 10.5194/gmd-12-1541-2019
- 418 Palter, J. B. (2015). The Role of the Gulf Stream in European Climate. *Annual Re-*  
 419 *view of Marine Science*, 7(1), 113–137. Retrieved from [https://doi.org/10](https://doi.org/10.1146/annurev-marine-010814-015656)  
 420 [.1146/annurev-marine-010814-015656](https://doi.org/10.1146/annurev-marine-010814-015656) doi: 10.1146/annurev-marine-010814-  
 421 -015656
- 422 Rahmstorf, S. (2002). Ocean circulation and climate during the past 120,000 years.  
 423 *Nature*, 419(6903), 207–214. Retrieved from [https://doi.org/10.1038/](https://doi.org/10.1038/nature01090)  
 424 [nature01090](https://doi.org/10.1038/nature01090) doi: 10.1038/nature01090
- 425 Schmittner, A., & Galbraith, E. D. (2008). Glacial greenhouse-gas fluctuations con-  
 426 trolled by ocean circulation changes. *Nature*, 456(7220), 373–376. Retrieved  
 427 from <https://doi.org/10.1038/nature07531> doi: 10.1038/nature07531
- 428 Sinet, S., von der Heydt, A. S., & Dijkstra, H. A. (2023, jan). AMOC Stabilization  
 429 Under the Interaction With Tipping Polar Ice Sheets. *Geophysical Research*  
 430 *Letters*, 50(2), e2022GL100305. Retrieved from [https://doi.org/10.1029/](https://doi.org/10.1029/2022GL100305)  
 431 [2022GL100305](https://doi.org/10.1029/2022GL100305) doi: <https://doi.org/10.1029/2022GL100305>
- 432 Sun, Y., Knorr, G., Zhang, X., Tarasov, L., Barker, S., Werner, M., & Lohmann, G.  
 433 (2022). Ice sheet decline and rising atmospheric CO<sub>2</sub> control AMOC sensitivity  
 434 to deglacial meltwater discharge. *Global and Planetary Change*, 210, 103755.

- 435 Retrieved from <https://www.sciencedirect.com/science/article/pii/S0921818122000224> doi: <https://doi.org/10.1016/j.gloplacha.2022.103755>
- 436
- 437 van der Ploeg, R., Cramwinckel, M. J., Kocken, I. J., Leutert, T. J., Bohaty, S. M.,
- 438 Fokkema, C. D., ... Sluijs, A. (2023). North Atlantic surface ocean warming
- 439 and salinization in response to middle Eocene greenhouse warming. *Science*
- 440 *Advances*, 9(4), eabq0110. Retrieved from <https://www.science.org/doi/abs/10.1126/sciadv.abq0110> doi: 10.1126/sciadv.abq0110
- 441
- 442 Vellinga, M., & Wood, R. A. (2002). Global Climatic Impacts of a Collapse of the
- 443 Atlantic Thermohaline Circulation. *Climatic Change*, 54(3), 251–267. Re-
- 444 trieved from <https://doi.org/10.1023/A:1016168827653> doi: 10.1023/A:
- 445 1016168827653
- 446 Vellinga, M., & Wood, R. A. (2008). Impacts of thermohaline circulation
- 447 shutdown in the twenty-first century. *Climatic Change*, 91(1), 43–63.
- 448 Retrieved from <https://doi.org/10.1007/s10584-006-9146-y> doi:
- 449 10.1007/s10584-006-9146-y
- 450 Weijer, W., Cheng, W., Drijfhout, S. S., Fedorov, A. V., Hu, A., Jackson, L. C., ...
- 451 Zhang, J. (2019, aug). Stability of the Atlantic Meridional Overturning Cir-
- 452 culation: A Review and Synthesis. *Journal of Geophysical Research: Oceans*,
- 453 124(8), 5336–5375. Retrieved from <https://doi.org/10.1029/2019JC015083>
- 454 doi: <https://doi.org/10.1029/2019JC015083>
- 455 Weijer, W., Cheng, W., Garuba, O. A., Hu, A., & Nadiga, B. T. (2020, jun).
- 456 CMIP6 Models Predict Significant 21st Century Decline of the Atlantic
- 457 Meridional Overturning Circulation. *Geophysical Research Letters*, 47(12),
- 458 e2019GL086075. Retrieved from <https://doi.org/10.1029/2019GL086075>
- 459 doi: <https://doi.org/10.1029/2019GL086075>
- 460 Weiss, R. F. (1974). Carbon dioxide in water and seawater: the solubility
- 461 of a non-ideal gas. *Marine Chemistry*, 2(3), 203–215. Retrieved from
- 462 <https://www.sciencedirect.com/science/article/pii/0304420374900152>
- 463 doi: [https://doi.org/10.1016/0304-4203\(74\)90015-2](https://doi.org/10.1016/0304-4203(74)90015-2)
- 464 Williams, R. G., & Follows, M. J. (2011). *Ocean Dynamics and the Carbon Cycle: Principles and Mechanisms*. Cambridge: Cambridge University Press. Re-
- 465 trieved from [https://www.cambridge.org/core/books/ocean-dynamics](https://www.cambridge.org/core/books/ocean-dynamics-and-the-carbon-cycle/31EF28FEF48A172FF746B3E654F9455A)
- 466 [-and-the-carbon-cycle/31EF28FEF48A172FF746B3E654F9455A](https://www.cambridge.org/core/books/ocean-dynamics-and-the-carbon-cycle/31EF28FEF48A172FF746B3E654F9455A) doi:
- 467 DOI:10.1017/CBO9780511977817
- 468
- 469 Wunderling, N., Donges, J. F., Kurths, J., & Winkelmann, R. (2021). In-
- 470 teracting tipping elements increase risk of climate domino effects under
- 471 global warming. *Earth System Dynamics*, 12(2), 601–619. Retrieved
- 472 from <https://esd.copernicus.org/articles/12/601/2021/> doi:
- 473 10.5194/esd-12-601-2021
- 474 Zeebe, R. E., Zachos, J. C., & Dickens, G. R. (2009). Carbon dioxide forcing alone
- 475 insufficient to explain Palaeocene–Eocene Thermal Maximum warming. *Nature Geoscience*, 2(8), 576–580. Retrieved from <https://doi.org/10.1038/ngeo578> doi: 10.1038/ngeo578
- 476
- 477
- 478 Zhang, X., Knorr, G., Lohmann, G., & Barker, S. (2017). Abrupt North At-
- 479 lantic circulation changes in response to gradual CO<sub>2</sub> forcing in a glacial
- 480 climate state. *Nature Geoscience*, 10(7), 518–523. Retrieved from
- 481 <https://doi.org/10.1038/ngeo2974> doi: 10.1038/ngeo2974

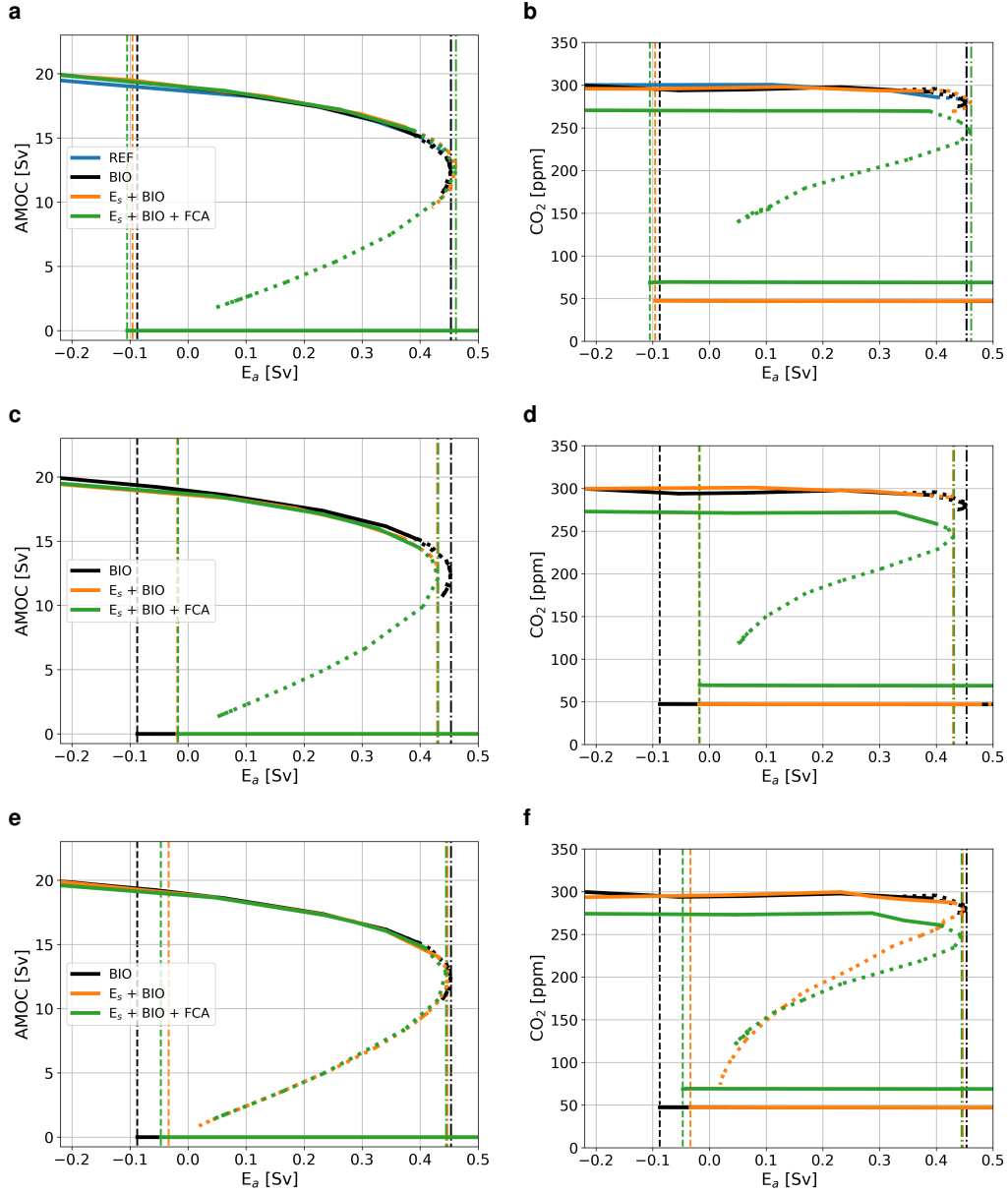


**Figure 2.** Bifurcation diagram showing the sensitivity of the AMOC to  $E_a$ . Solid lines represent stable steady state solutions, dotted lines represent unstable solutions, dash-dotted lines represent the location of the saddle node on the on-branch, and dashed lines the location of the saddle node on the off-branch. The blue lines represent a case without biological,  $E_s$ - $pCO_2$  and rain ratio coupling (REF), the black lines with only the biological coupling (BIO), the orange lines with the linear CMIP6 based  $E_s$  and biological coupling ( $E_s + BIO$ ), and the green lines represent a case where also the rain ratio feedback is applied ( $E_s + BIO + FCA$ ). Results are for the AMOC strength in Sv (a) and atmospheric  $pCO_2$  in ppm (b). Case REF is difficult to see in A because it is similar to case BIO except that it does not simulate an off-branch. Panels a and b are for Eq. 1, panels c and d are for Eq. 2 and panels e and f are for Eq. 3. In a, b, c and d the orange saddle node lines are located behind the green lines.

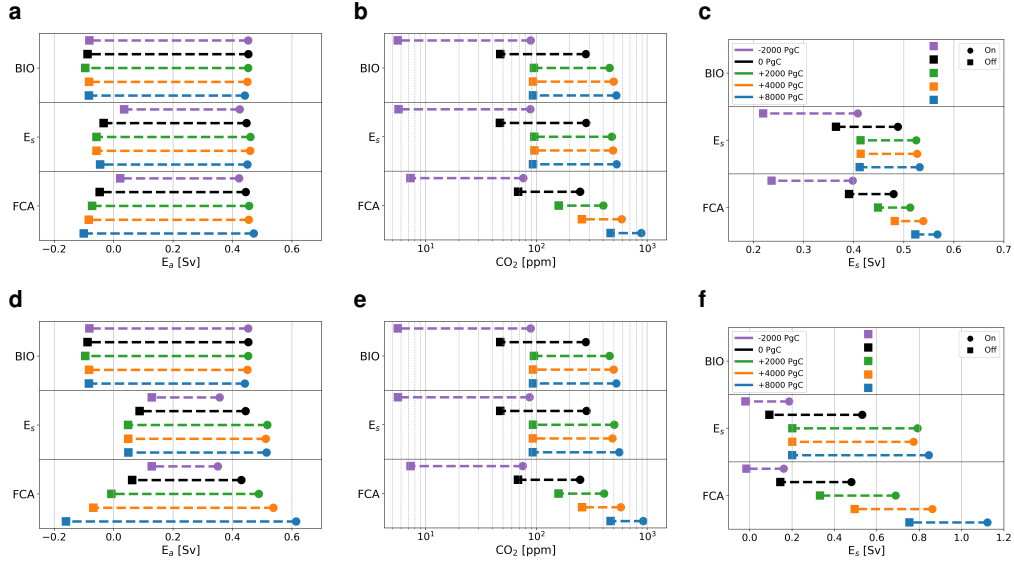


**Figure 3.** Panel a shows the location of the saddle nodes versus  $E_a$  in Sv, panel b shows the corresponding  $\text{CO}_2$  concentration in ppm (note that the x-axis is logarithmic), and c shows the corresponding value of  $E_s$  in Sv following Eq. 2. In A-C the top of the figure represents case BIO, the middle case  $E_s + \text{BIO}$ , and the bottom case  $E_s + \text{BIO} + \text{FCA}$ . Square markers represent the location of the saddle node on the off-branch and round markers the location of the saddle node on the on-branch for cases where 4000 PgC is removed (purple), 2000 PgC is removed (black), the default carbon content (green), 4000 PgC is added (orange) and where 8000 PgC is added (blue) to the the standard case considered in Fig. 2. Panels d-f are as in a-c but for the  $E_s$  coupling in Eq. 3.

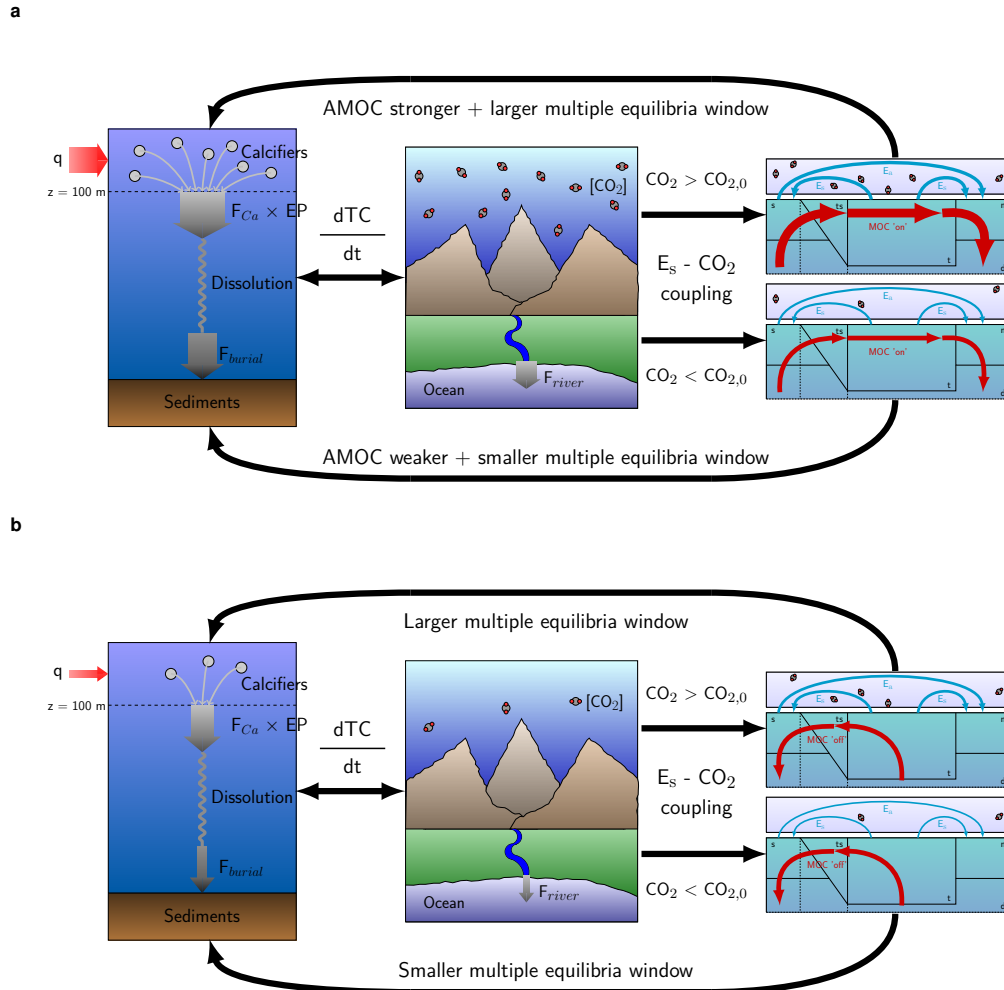


**Figure 4.** Illustrations of the main mechanisms affecting atmospheric  $pCO_2$  and AMOC stability. Panel a shows the mechanisms for the on-branch. A strong AMOC increases export production through increased nutrient advection (left panel), which is accompanied by a high atmospheric  $pCO_2$  due to the necessary balance between the river influx and sediment burial (middle panel). If the  $CO_2$  concentration is larger (smaller) than  $CO_{2,0}$  than the AMOC will strengthen (weaken) and the MEW increases (decreases) (right panels). Panel b shows the mechanisms for the off-branch. The absence of an AMOC decreases export production through decreased nutrient advection (left panel), accompanied by a low atmospheric  $pCO_2$  (middle panel). When  $pCO_2$  is larger (smaller) than  $pCO_{2,0}$  the MEW increases (decreases) (right panel).



**Abstract**

The Atlantic Meridional Overturning Circulation (AMOC) is considered to be a tipping element in the Earth System with multiple stable states. Here, we investigate the multiple equilibria window of the AMOC within a coupled ocean circulation-carbon cycle box model. We show that adding couplings between the ocean circulation and the carbon cycle model affects the multiple equilibria window of the AMOC. Increasing the total carbon content of the system will widen the multiple equilibria window of the AMOC, since higher atmospheric  $p\text{CO}_2$  values are accompanied by stronger freshwater forcing over the Atlantic ocean which acts to increase the window. Our results suggest that future changes in the marine carbon cycle can influence AMOC stability in future climates.

**Plain Language Summary**

The Atlantic Meridional Overturning Circulation (AMOC), an important circulation system in the Earth System, is considered to be a tipping element with multiple stable states. In this study we investigate the range in which these multiple stable states exist, termed the multiple equilibria window, with a simple coupled ocean circulation-carbon cycle box model. We show that depending on the coupling between the ocean circulation model and the carbon cycle model, the multiple equilibria window of the AMOC changes, where it can become both smaller and larger. Furthermore, we also show that when total carbon content in the ocean-atmosphere system is increased, the width of the multiple equilibria window is increased. These results suggest that the marine carbon cycle has influenced AMOC stability in past climates, and can influence it in future climates.

**1 Introduction**

The Atlantic Meridional Overturning Circulation (AMOC) transports heat from the Southern to the Northern Hemisphere and thereby plays a large role in modulating global climate (Vellinga & Wood, 2008; Palter, 2015). It is one of the prominent tipping elements in the Earth System (Lenton et al., 2008; McKay et al., 2022). Model studies suggest that the AMOC has multiple stable states: the on-state, representing the current AMOC state with a strong northward flow at the surface and a southward return flow at intermediate depth; and the off-state, representing a weak or even reversed AMOC state (Weijer et al., 2019). From a dynamical systems point of view, a bi-stable AMOC regime appears through the occurrence of two saddle node bifurcations (Dijkstra, 2007) and the region in parameter space where both on- and off-states co-exist is the multiple equilibria window (MEW), also referred to as the bi-stability window (Barker & Knorr, 2021).

Climate variability in the past, such as Heinrich events, has been linked to tipping of the AMOC (Rahmstorf, 2002; Lynch-Stieglitz, 2017). Under anthropogenic forcing, the global warming threshold for AMOC tipping has been recently estimated to be around  $4^\circ\text{C}$  (McKay et al., 2022). Model data from the Coupled Model Intercomparison Project 6 (CMIP6; Eyring et al., 2016), Weijer et al. (2020) project a consistent weakening of the AMOC under future climate change, with a 34-45% decrease in AMOC strength in 2100, but no clear tipping was found. However, these models may have a too stable AMOC (Weijer et al., 2019) and the probability of AMOC tipping before 2100 may still be non-negligible. Under AMOC tipping, a strong cooling in the Northern Hemisphere (Rahmstorf, 2002; Drijfhout, 2015), changes in the water cycle (Vellinga & Wood, 2002; Jackson et al., 2015), and potential interactions with other tipping elements in the Earth System (Dekker et al., 2018; Wunderling et al., 2021; Sinet et al., 2023) are expected.

The AMOC can also interact with the marine carbon cycle and therefore influence atmospheric  $p\text{CO}_2$ . By affecting the transport of important tracers, such as dissolved

inorganic carbon (DIC), total alkalinity, and nutrients, the AMOC affects the solubility and biological carbon pumps. Evidence for a coupling between the AMOC and marine carbon cycle is provided in proxy data (Bauska et al., 2021). Model studies show a wide range of potential carbon cycle responses to a collapse of the AMOC. While most models show an increase in atmospheric  $p\text{CO}_2$  (e.g. Marchal et al., 1998; Schmittner & Galbraith, 2008; Matsumoto & Yokoyama, 2013), the magnitude and precise mechanisms are dependent on the model used and climatic boundary conditions (Gottschalk et al., 2019).

As the AMOC can influence atmospheric  $p\text{CO}_2$ , there is a potential feedback mechanism since  $\text{CO}_2$  influences the hydrological cycle (Weijer et al., 2019; Barker & Knorr, 2021) and, through changes in buoyancy fluxes, affects the AMOC. Previous studies suggest that there may be a relation between atmospheric  $p\text{CO}_2$  and the MEW of the AMOC (Barker et al., 2010, 2015). However, a clear mechanistic view has not been given yet. Here, we study the mechanisms on how the marine carbon cycle affects the MEW of the AMOC using a coupled Atlantic Ocean circulation-carbon cycle box model.

## 2 Method

We couple an Atlantic Ocean circulation model (Cimatoribus et al., 2014; Castellana et al., 2019) to a carbon cycle model (O'Neill et al., 2019; Boot et al., 2022). The ocean circulation model (Fig. 1) simulates the distribution of salinity in 5 ocean boxes and the depth of the pycnocline in the Atlantic Ocean and is well suited to simulate AMOC dynamics (Cimatoribus et al., 2014). Salinity in the model is affected by wind and buoyancy driven ocean flows and by freshwater fluxes. The carbon-cycle model simulates DIC, alkalinity (Alk) and phosphate ( $\text{PO}_4$ ) and captures relevant processes such as riverine input, air-sea gas exchange, biological export production,  $\text{CaCO}_3$  rain,  $\text{CaCO}_3$  dissolution and sediment burial (Fig. 1). The AMOC influences the carbon cycle directly by advective transport of the tracers and the simulated salt distributions in the AMOC model are used as input for the carbonate chemistry and tracer transport in the carbon-cycle model. An important coupling between both models is due to the fact that biological export production is dependent on nutrient transport. By representing the symmetrical component of the freshwater forcing  $E_s$  of the AMOC model (Fig. 1) as a function of atmospheric  $p\text{CO}_2$ , another important coupling between both models is represented.

To determine the functional relation between  $p\text{CO}_2$  and  $E_s$ , we use a fit from a CMIP6 multi-model mean, based on 28 models, simulated under the 1%  $\text{CO}_2$  increase scenario (Eyring et al., 2016). We fit both a linear and logarithmic function to atmospheric  $p\text{CO}_2$  data and the freshwater flux into the ocean region represented by the thermocline box in our model (box  $t$  in Fig. 1). There is net evaporation over this region which represents  $2 E_s$  in the box model resulting in the linear (Eq. 1) and logarithmic (Eq. 2) fits shown in Figure S1. We will use both fits in section 3.1 since the fits show different behavior for  $p\text{CO}_2$  values lower than 300 ppm, and by using both we test the sensitivity of the model to the used fit. The fits (in Sv) are given by:

$$E_s = 0.562 + 0.00012 \times p\text{CO}_2 \quad (1)$$

$$E_s = 0.099 + 0.079 \times \ln(p\text{CO}_2) \quad (2)$$

Both relations above capture the effect of  $\text{CO}_2$  induced warming on the hydrological cycle that results in the subtropical regions becoming drier under higher  $p\text{CO}_2$  values, while sub-polar regions become wetter, which is indeed seen in both model and paleo proxy studies (Held & Soden, 2006; Bonfils et al., 2020; van der Ploeg et al., 2023).

The relations (Eq. 1) and (Eq. 2) could only be determined from the CMIP6 models over a limited range of  $p(\text{CO}_2)$  and only for time varying climates. To extend that

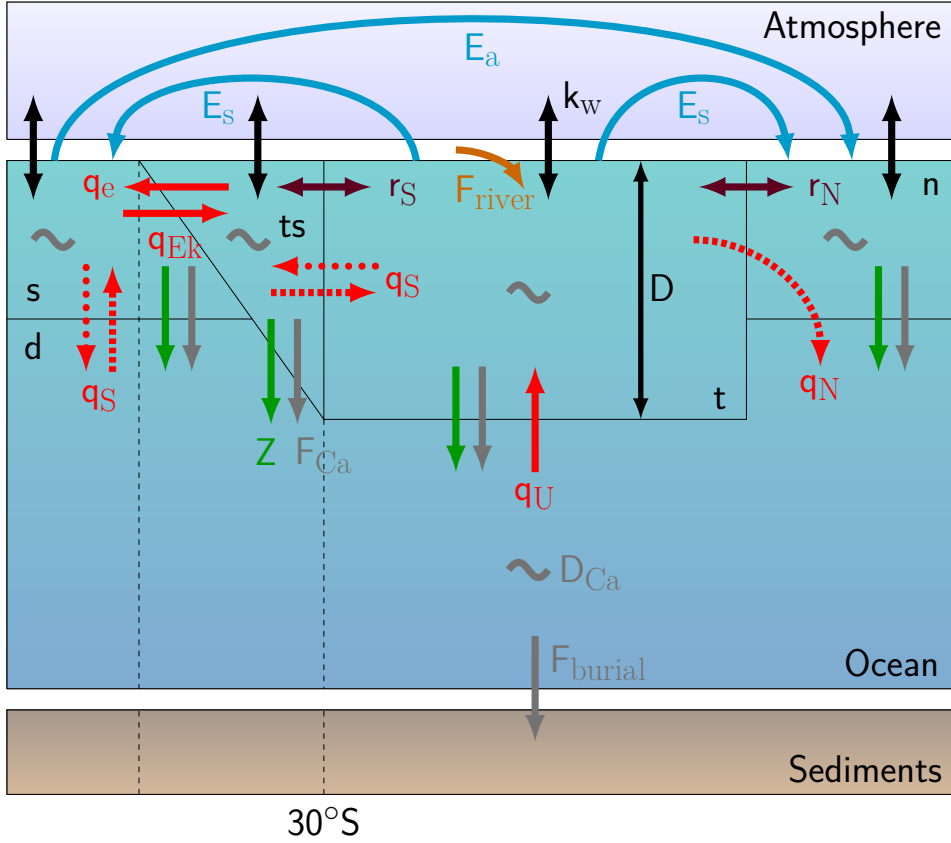


**Figure 1.** Box structure and processes simulated in the coupled circulation – carbon cycle model. Red arrows represent volume transports where dashed arrows are only present during an on-state, and dotted arrows only present during an off-state. The purple arrows represent gyre exchange ( $r_N$  and  $r_S$ ), and blue arrows freshwater fluxes ( $E_s$  for the symmetrical forcing, and  $E_a$  for the asymmetrical forcing). Carbon cycle processes that are represented are riverine input (orange), air-sea gas exchange (black;  $k_w$ ), biological export production (green;  $Z$ ),  $\text{CaCO}_3$  rain (grey;  $F_{Ca}$ ),  $\text{CaCO}_3$  dissolution (grey;  $D_{Ca}$ ), and sediment burial (grey;  $F_{burial}$ ). Based on Castellana et al. (2019) and Boot et al. (2022).

112 range and to capture the possibility that the fits (Eq.1 and 2) do not accurately repre-  
 113 sent the  $E_s$ - $p\text{CO}_2$ -coupling in steady state climates, we also use a third relation

$$E_s = 0.1 + 0.75 \times \ln\left(\frac{p\text{CO}_2 + 250}{p\text{CO}_{2,0}}\right) \quad (3)$$

114 to demonstrate the effect of the carbon cycle on the AMOC MEW for a larger range of  
 115 possible  $E_s$ - $p\text{CO}_2$  coupling strengths. The parameter values in (Eq. 3) are tuned such  
 116 that  $E_s$  approaches 0 when atmospheric  $p\text{CO}_2$  approaches 0, and that  $E_s = E_{s,base}$  (0.56 Sv)  
 117 when atmospheric  $p\text{CO}_2$  is equal to  $p\text{CO}_{2,0} = 300$  ppm. When the  $\text{CO}_2$  concentration  
 118 exceeds  $p\text{CO}_{2,0}$ ,  $E_s$  will be larger than  $E_{s,base}$ . Both logarithmic fits (Eq. 2 and Eq. 3)  
 119 are used in sections 3.1 and 3.2.

### 3 Results

The equations of the coupled model (see Supporting Information) are implemented in the continuation software AUTO-07p (Doedel et al., 2007), which is able to efficiently compute branches of steady state solutions in parameter space and to detect the saddle-node bifurcations bounding the MEW. For the AMOC bifurcation diagram, we use the asymmetric component of the freshwater flux  $E_a$  as a control parameter as in Castellana et al. (2019). In the results below, we will consider four different cases of the model related to capturing different carbon-cycle processes. In case REF we use the default coupled circulation-carbon cycle model. In BIO we add the coupling of export production to the ocean circulation. In BIO+ $E_s$ , the  $E_s$ -pCO<sub>2</sub> coupling is added, and lastly, in case BIO+ $E_s$ +FCA, the rain ratio is modelled as a function of the calcium carbonate (CaCO<sub>3</sub>) saturation state, whereas in the other three cases it is constant (see also Table S1 for the specifics of the different cases).

#### 3.1 The AMOC multiple equilibria window

The bifurcation diagrams, showing the AMOC strength versus  $E_a$  are for the three  $E_s$ -pCO<sub>2</sub> relations (Eq. 1), (Eq. 2) and (Eq. 3) in Fig. 2a-b, Fig. 2c-d and Fig. 2e-f, respectively.

To be able to simulate both the on- and off-branch in the coupled model, it is vital that the BIO coupling is used, since otherwise phosphate concentration in the surface ocean will become negative under a collapsed AMOC regime. This behavior is illustrated in Fig. 2a, b by the cases REF and BIO. In case REF the off-branch is not shown, while for case BIO the full bifurcation diagram with two saddle-node bifurcations is plotted. Atmospheric pCO<sub>2</sub> also shows hysteresis behavior with low concentrations on the off-branch (around 50 ppm).

To explain the low pCO<sub>2</sub> values on- the off-branch we look at the constraint in the model on total carbon content in the ocean-atmosphere system. In steady state, the riverine input and sediment outflux of DIC must balance to keep the total carbon content constant (in time). In our model, the sediment outflux is a function of the saturation state of CaCO<sub>3</sub> and CaCO<sub>3</sub> flux which is a function of the rain ratio (constant in non-FCA cases) and the export production. However, in this model set up, the saturation state of CaCO<sub>3</sub> in the ocean is in every box larger than 1, meaning that there is no saturation driven dissolution of CaCO<sub>3</sub> and the sediment outflux is purely a function of the export production. In an AMOC off-state, nutrient advection is low causing a large reduction in export production, and therefore a small sediment outflux. The riverine influx must balance this small outflux, which can only be achieved by decreasing atmospheric pCO<sub>2</sub> to the values reported on the off-branch. When the rain ratio feedback is used (case FCA), this mechanism is also present, but the sediment outflux is in this case also a function of the rain ratio. In the FCA case, the rain ratio is variable when the saturation state of CaCO<sub>3</sub> is larger than 1. This results in larger rain ratio values, and therefore more CaCO<sub>3</sub> export to the sediments increasing the sediment outflux and, through the river influx, atmospheric pCO<sub>2</sub>.

When the linear CMIP6  $E_s$ -pCO<sub>2</sub> coupling (Eq. 1) is used, the MEW increases slightly. The saddle node on the on-branch shifts from 0.45Sv to 0.46Sv, and the saddle node on the off-branch shifts from -0.08Sv to -0.10Sv for both  $E_s$ +BIO and  $E_s$ +BIO+FCA. Due to the presence of a subcritical Hopf bifurcation in the AMOC model, the on-branch becomes unstable before the saddle node. The presence of the Hopf bifurcation is not further considered in this study as we are only interested in the MEW. The small movement of the saddle nodes in parameter space shows that when the linear CMIP6 fit is used, the CO<sub>2</sub> dependency of  $E_s$  is too weak to significantly impact the MEW. When the logarithmic CMIP6 fit (Eq. 2) is used, the MEW becomes smaller (Fig. 2c, d). The logarithmic fit (Eq. 3) over the full pCO<sub>2</sub> range shows that the marine carbon cycle can

171 have a substantial effect on the AMOC MEW, as the saddle node on the off-branch moves  
 172 to larger values of  $E_a$ .

173 To explain the movement of the saddle nodes, we consider the sensitivity of the model  
 174 to  $E_s$  (Figure S1). The default value used for cases REF and BIO for  $E_s$  is 0.56 Sv. The  
 175 logarithmic CMIP6 fit results in a slightly smaller value, whereas the linear fit has a slightly  
 176 larger value. Due to increased  $E_s$ , the thermocline becomes saltier, and in combination  
 177 with the salt-advection feedback, this leads to a larger meridional density gradient and  
 178 therefore a stronger AMOC. Furthermore, increased  $E_s$  increases the net evaporation over  
 179 the Atlantic, given by  $(E_s - E_a)$  and a larger  $E_a$  is necessary to tip the AMOC. On the  
 180 off-branch, a larger  $E_s$  results in salinification of the  $ts$  box and a more negative fresh-  
 181 water flux ( $E_a$ ) is needed to increase the meridional density gradient and reinvigorate  
 182 the AMOC. This behavior of the AMOC model explains the differences between Figs.  
 183 2a-b and 2c-d. The fit Eq. 3 narrows the MEW by moving the saddle node on the off-  
 184 branch to larger values of  $E_a$  (Fig. 2e, f). Using this fit shows more clearly that there  
 185 can be an influence on the MEW via a coupling to atmospheric  $pCO_2$ . Here, it reduces  
 186 the MEW by moving the off-branch saddle node to larger values of  $E_a$  which can be ex-  
 187 plained by the fact that  $CO_2$  on the off-branch is smaller than  $CO_{2,0}$  and therefore  $E_s$   
 188 is smaller than  $E_{s,base}$ .

### 189 3.2 Sensitivity to total carbon content

190 Over the Cenozoic, both the AMOC (Lynch-Stieglitz, 2017) and total carbon con-  
 191 tent in the ocean-atmosphere system have varied (Zeebe et al., 2009; Caves et al., 2016).  
 192 In Caves et al. (2016) it is suggested that total carbon content has varied between 24,000  
 193 PgC and 96,000 PgC. In the previous section, the model was studied with approximately  
 194 8000 PgC in the Atlantic and Southern Ocean which translates to approximately 40,000  
 195 PgC in the global system (since our model represents approximately 20% of the global  
 196 ocean). In this section, we analyze how the sensitivity to  $E_a$  changes under different to-  
 197 tal carbon contents in the model. To test the sensitivity, we remove approximately 2000  
 198 (-25%) PgC, and add approximately 2000 (+25%), 4000 (+50%) and 8000 (+100%) PgC.  
 199 We do this for the CMIP6 logarithmic coupling (Eq. 2; Fig. 3a-c) and the strong log-  
 200 arithmic coupling (Eq. 3; Fig. 3d-f). Both cases show similar results, but in Fig. 3a-c  
 201 the MEW changes are less pronounced; we therefore focus on the results in Fig. 3d-f.

202 The MEW increases when total carbon increases. There is, however, a different re-  
 203 sponse when the rain ratio feedback (FCA) is included. For case  $E_s$ +BIO we see that  
 204 the MEW increases under a total C change from -2000 PgC to +2000 PgC, but then re-  
 205 mains constant for more carbon content. We can explain this by looking at the atmo-  
 206 spheric  $pCO_2$  values, and therefore also  $E_s$ , at the saddle node, which are similar for the  
 207 three high carbon cases. When the rain ratio feedback is used, we see that the MEW keeps  
 208 increasing for larger carbon contents since also the atmospheric  $pCO_2$  increases. We can  
 209 explain the difference between  $E_s$ +BIO and  $E_s$ +BIO+FCA by the constraint on total  
 210 carbon in the ocean-atmosphere system. In  $E_s$ +BIO, biological export production is mainly  
 211 a function of the AMOC strength, whereas in the  $E_s$ +BIO+FCA case it is also depen-  
 212 dent on the  $CaCO_3$  saturation state which is coupled to atmospheric  $pCO_2$  through the  
 213 pH of the surface ocean. This increases the biological export production, and through  
 214 the same mechanisms as described before, higher atmospheric  $pCO_2$  values.

## 215 4 Summary and discussion

216 In this paper we investigated the multiple equilibria window (MEW) of the AMOC  
 217 in a coupled ocean circulation-carbon cycle box model. When freshwater forcing is cou-  
 218 pled to atmospheric  $pCO_2$  using CMIP6 multi-model fits (Eq. 1 and Eq. 2), the MEW  
 219 changes slightly due to a weak dependency on atmospheric  $pCO_2$ . However, when we  
 220 use a stronger coupling (Eq. 3), the saddle node on the off-branch moves towards larger

221  $E_a$  values and thereby reduces the MEW. We also assessed the sensitivity to total car-  
 222 bon content in the system and found that the MEW is larger with more carbon in the  
 223 system due to a shift of both the on- and off-branch saddle nodes. Both results show the  
 224 potential of the marine carbon cycle to influence the MEW of the AMOC.

225 We acknowledge that it is difficult to provide an adequate justification of the dif-  
 226 ferent  $E_s$ - $p\text{CO}_2$  relations because the CMIP6 model  $p\text{CO}_2$  range is too small and there  
 227 are no observations which can test the strong coupling relation (Eq. 3). However, from  
 228 the results clear and plausible mechanisms can be extracted which cause the change in  
 229 MEW and these are more important than the precise quantitative estimates. Two pro-  
 230 cesses explain the results on the MEW: (1) the balance between the river flux and sed-  
 231 iment flux that constrains atmospheric  $p\text{CO}_2$ ; and (2) the sensitivity of the AMOC to  
 232  $E_s$ . In the model, atmospheric  $p\text{CO}_2$  is dependent on the ocean circulation through ex-  
 233 port production,  $E_s$  is dependent on atmospheric  $p\text{CO}_2$ , and the ocean circulation is de-  
 234 pendent on  $E_s$ , creating a feedback loop (Fig. 4). We see that when atmospheric  $p\text{CO}_2$   
 235 is high, so is  $E_s$  which results in a stronger AMOC on the on-branch. As a consequence,  
 236 export production is increased and there will be a larger outflux of carbon and alkalini-  
 237 ty through the sediments, which is balanced by a high influx of carbon through the rivers,  
 238 consistent with high atmospheric  $p\text{CO}_2$  values. Of the feedbacks that we have implemented,  
 239 only the rain ratio feedback (FCA) affects this mechanism because it directly influences  
 240 the sediment outflux and makes the carbon cycle less sensitive to the ocean circulation.  
 241

242 The results here can be relevant when studying climate transitions in past and fu-  
 243 ture climates as it identifies mechanisms how AMOC stability can depend on background  
 244 climate and atmospheric  $p\text{CO}_2$  values. Previous work focused on the Pleistocene sug-  
 245 gest an influence of atmospheric  $p\text{CO}_2$  on the stability structure of the AMOC through  
 246 temperature (Sun et al., 2022) and moisture transport (Zhang et al., 2017). In our model,  
 247 there is no effect of temperature changes, but the  $E_s$  coupling used here is similar to the  
 248 moisture transport described in Zhang et al. (2017) the only difference being that this  
 249 moisture transport is to the Pacific basin, whereas in our model it is redistributed over  
 250 the Atlantic to conserve salinity.

251 We have used a model that provides a simple framework for studying AMOC dy-  
 252 namics that allows us to efficiently test the concept of AMOC stability in a wide range  
 253 of parameter values. However, a limitation is that the model only represents a fifth of  
 254 the global ocean, the Atlantic and Southern Ocean. For the circulation model this might  
 255 not be a large deficiency, but for the carbon cycle model it might be. Furthermore, the  
 256 coupled model might not be valid for the entire parameter space we have simulated. An  
 257 example of this, is the unrealistic low  $p\text{CO}_2$  values on the off-branch. These low values  
 258 suggest that some important processes are missing, e.g. negative feedbacks arising in the  
 259 Indo-Pacific basin or in the terrestrial biosphere. Though not a limitation in the model,  
 260 it is good to note that the range of timescales in the carbon cycle model is larger than  
 261 in the circulation model, which does not affect our results but does affect the time de-  
 262 pendent response of the system.

263 Our work also holds implications for assessing AMOC stability in future climates.  
 264 Currently, the global warming threshold for an AMOC collapse is estimated to be 4 °C  
 265 (McKay et al., 2022). In the future, the carbon content of the ocean-atmosphere system  
 266 will increase, potentially increasing the MEW which can change the likelihood of a bi-  
 267 furcation induced AMOC collapse. In this study we focused on slow, bifurcation induced  
 268 tipping of the AMOC, while the AMOC is also able to tip due to faster processes result-  
 269 ing in noise-induced tipping (Castellana et al., 2019). We hope this work inspires fur-  
 270 ther research on the dependency of the MEW of the AMOC on the carbon cycle in more  
 271 detailed models to further investigate the relevance of the mechanism found in this study  
 272 and provide a quantification for the influence of the marine carbon cycle on the MEW  
 273 of the AMOC.

274 **Appendix A Open Science**

275 Model code, generated model data, scripts for plotting all figures can be found at  
 276 10.5281/zenodo.8042693 (Boot et al., 2023). A list of used datasets, processed datasets  
 277 and citations for the CMIP6 multi-model fits is also included in this repository. CMIP6  
 278 model data can be downloaded from the Earth System Grid Federation (ESGF) ([https://  
 279 esgf-node.llnl.gov/search/cmip6/](https://esgf-node.llnl.gov/search/cmip6/)). AUTO-07p can be downloaded from [https://  
 280 github.com/auto-07p](https://github.com/auto-07p).

281 **Acknowledgments**

282 This study has been supported by the Netherlands Earth System Science Centre (NESSC),  
 283 which is financially supported by the Ministry of Education, Culture and Science (OCW;  
 284 grant no. 024.002.001)

285 **References**

- 286 Andersson, A., Graw, K., Schröder, M., Fennig, K., Liman, J., Bakan, S., ... Klepp,  
 287 C. (2017). *Hamburg Ocean Atmosphere Parameters and Fluxes from Satel-  
 288 lite Data - HOAPS 4.0*. Satellite Application Facility on Climate Monitor-  
 289 ing (CM SAF). Retrieved from [https://wui.cmsaf.eu/safira/action/  
 290 viewDoiDetails?acronym=HOAPS{\\\_}V002](https://wui.cmsaf.eu/safira/action/viewDoiDetails?acronym=HOAPS{\_}V002) doi: 10.5676/EUM.SAF\_CM/  
 291 HOAPS/V002
- 292 Barker, S., Chen, J., Gong, X., Jonkers, L., Knorr, G., & Thornalley, D. (2015). Ice-  
 293 bergs not the trigger for North Atlantic cold events. *Nature*, *520*(7547), 333–  
 294 336. Retrieved from <https://doi.org/10.1038/nature14330> doi: 10.1038/  
 295 nature14330
- 296 Barker, S., & Knorr, G. (2021). Millennial scale feedbacks determine the shape and  
 297 rapidity of glacial termination. *Nature Communications*, *12*(1), 2273. Re-  
 298 trieved from <https://doi.org/10.1038/s41467-021-22388-6> doi: 10.1038/  
 299 s41467-021-22388-6
- 300 Barker, S., Knorr, G., Vautravers, M. J., Diz, P., & Skinner, L. C. (2010). Extreme  
 301 deepening of the Atlantic overturning circulation during deglaciation. *Na-  
 302 ture Geoscience*, *3*(8), 567–571. Retrieved from [https://doi.org/10.1038/  
 303 ngeo921](https://doi.org/10.1038/ngeo921) doi: 10.1038/ngeo921
- 304 Bauska, T. K., Marcott, S. A., & Brook, E. J. (2021). Abrupt changes in the global  
 305 carbon cycle during the last glacial period. *Nature Geoscience*, *14*(2), 91–  
 306 96. Retrieved from <https://doi.org/10.1038/s41561-020-00680-2> doi:  
 307 10.1038/s41561-020-00680-2
- 308 Bonfils, C. J. W., Santer, B. D., Fyfe, J. C., Marvel, K., Phillips, T. J., & Zim-  
 309 merman, S. R. H. (2020). Human influence on joint changes in tempera-  
 310 ture, rainfall and continental aridity. *Nature Climate Change*, *10*(8), 726–  
 311 731. Retrieved from <https://doi.org/10.1038/s41558-020-0821-1> doi:  
 312 10.1038/s41558-020-0821-1
- 313 Boot, A., von der Heydt, A. S., & Dijkstra, H. A. (2022). Effect of the At-  
 314 lantic Meridional Overturning Circulation on atmospheric  $\text{CO}_2$   
 315 variations. *Earth System Dynamics*, *13*(3), 1041–1058. Retrieved from  
 316 <https://esd.copernicus.org/articles/13/1041/2022/> doi: 10.5194/  
 317 esd-13-1041-2022
- 318 Boot, A., von der Heydt, A. S., & Dijkstra, H. A. (2023, June). *AMOC MEW GRL*.  
 319 [dataset]. Zenodo. doi: 10.5281/zenodo.8042693
- 320 Castellana, D., Baars, S., Wubs, F. W., & Dijkstra, H. A. (2019). Transition Prob-  
 321 abilities of Noise-induced Transitions of the Atlantic Ocean Circulation. *Scien-  
 322 tific Reports*, *9*(1), 20284. Retrieved from [https://doi.org/10.1038/s41598-  
 323 -019-56435-6](https://doi.org/10.1038/s41598-019-56435-6) doi: 10.1038/s41598-019-56435-6
- 324 Caves, J. K., Jost, A. B., Lau, K. V., & Maher, K. (2016). Cenozoic carbon cycle

- 325 imbalances and a variable weathering feedback. *Earth and Planetary Science*  
 326 *Letters*, *450*, 152–163. Retrieved from [https://www.sciencedirect.com/](https://www.sciencedirect.com/science/article/pii/S0012821X16303223)  
 327 [science/article/pii/S0012821X16303223](https://www.sciencedirect.com/science/article/pii/S0012821X16303223) doi: [https://doi.org/10.1016/](https://doi.org/10.1016/j.epsl.2016.06.035)  
 328 [j.epsl.2016.06.035](https://doi.org/10.1016/j.epsl.2016.06.035)
- 329 Cimadoribus, A. A., Drijfhout, S. S., & Dijkstra, H. A. (2014). Meridional overturn-  
 330 ing circulation: stability and ocean feedbacks in a box model. *Climate Dynam-*  
 331 *ics*, *42*(1), 311–328. Retrieved from [https://doi.org/10.1007/s00382-012-](https://doi.org/10.1007/s00382-012-1576-9)  
 332 [1576-9](https://doi.org/10.1007/s00382-012-1576-9) doi: 10.1007/s00382-012-1576-9
- 333 Dekker, M. M., von der Heydt, A. S., & Dijkstra, H. A. (2018). Cascading transi-  
 334 tions in the climate system. *Earth System Dynamics*, *9*(4), 1243–1260. Re-  
 335 trieved from <https://esd.copernicus.org/articles/9/1243/2018/> doi: 10  
 336 .5194/esd-9-1243-2018
- 337 Dijkstra, H. A. (2007, oct). Characterization of the multiple equilibria regime in  
 338 a global ocean model. *Tellus A*, *59*(5), 695–705. Retrieved from [https://](https://doi.org/10.1111/j.1600-0870.2007.00267.x)  
 339 [doi.org/10.1111/j.1600-0870.2007.00267.x](https://doi.org/10.1111/j.1600-0870.2007.00267.x) doi: [https://doi.org/10.1111/](https://doi.org/10.1111/j.1600-0870.2007.00267.x)  
 340 [j.1600-0870.2007.00267.x](https://doi.org/10.1111/j.1600-0870.2007.00267.x)
- 341 Doedel, E. J., Paffenroth, R. C., Champneys, A. C., Fairgrieve, T. F., Kuznetsov,  
 342 Y. A., Oldeman, B. E., ... Wang, X. J. (2007). *AUTO-07p: Continuation and*  
 343 *Bifurcation Software for Ordinary Differential Equations*.
- 344 Drijfhout, S. (2015). Competition between global warming and an abrupt collapse of  
 345 the AMOC in Earth’s energy imbalance. *Scientific Reports*, *5*(1), 14877. Re-  
 346 trieved from <https://doi.org/10.1038/srep14877> doi: 10.1038/srep14877
- 347 Eyring, V., Bony, S., Meehl, G. A., Senior, C. A., Stevens, B., Stouffer, R. J., &  
 348 Taylor, K. E. (2016, may). Overview of the Coupled Model Intercompari-  
 349 son Project Phase 6 (CMIP6) experimental design and organization. *Geosci.*  
 350 *Model Dev.*, *9*(5), 1937–1958. Retrieved from [https://gmd.copernicus.org/](https://gmd.copernicus.org/articles/9/1937/2016/)  
 351 [articles/9/1937/](https://gmd.copernicus.org/articles/9/1937/2016/)  
 352 [https://gmd.copernicus.org/articles/9/1937/](https://gmd.copernicus.org/articles/9/1937/2016/gmd-9-1937-2016.pdf)  
 353 [2016/gmd-9-1937-2016.pdf](https://gmd.copernicus.org/articles/9/1937/2016/gmd-9-1937-2016.pdf) doi: 10.5194/gmd-9-1937-2016
- 354 Follows, M. J., Ito, T., & Dutkiewicz, S. (2006). On the solution of the carbonate  
 355 chemistry system in ocean biogeochemistry models. *Ocean Modelling*, *12*(3),  
 356 290–301. Retrieved from [http://www.sciencedirect.com/science/article/](http://www.sciencedirect.com/science/article/pii/S1463500305000533)  
 357 [pii/S1463500305000533](http://www.sciencedirect.com/science/article/pii/S1463500305000533) doi: <https://doi.org/10.1016/j.ocemod.2005.05.004>
- 358 Gottschalk, J., Battaglia, G., Fischer, H., Frölicher, T. L., Jaccard, S. L., Jeltsch-  
 359 Thömmes, A., ... Stocker, T. F. (2019). Mechanisms of millennial-scale  
 360 atmospheric CO<sub>2</sub> change in numerical model simulations. *Quaternary Sci-*  
 361 *ence Reviews*, *220*, 30–74. Retrieved from [http://www.sciencedirect.com/](http://www.sciencedirect.com/science/article/pii/S0277379118310473)  
 362 [science/article/pii/S0277379118310473](http://www.sciencedirect.com/science/article/pii/S0277379118310473) doi: [https://doi.org/10.1016/](https://doi.org/10.1016/j.quascirev.2019.05.013)  
 363 [j.quascirev.2019.05.013](https://doi.org/10.1016/j.quascirev.2019.05.013)
- 364 Held, I. M., & Soden, B. J. (2006). Robust Responses of the Hydrological Cy-  
 365 cle to Global Warming. *Journal of Climate*, *19*(21), 5686–5699. Re-  
 366 trieved from [https://journals.ametsoc.org/view/journals/clim/19/](https://journals.ametsoc.org/view/journals/clim/19/21/jcli3990.1.xml)  
 367 [21/jcli3990.1.xml](https://journals.ametsoc.org/view/journals/clim/19/21/jcli3990.1.xml) doi: 10.1175/JCLI3990.1
- 368 Jackson, L. C., Kahana, R., Graham, T., Ringer, M. A., Woollings, T., Mecking,  
 369 J. V., & Wood, R. A. (2015). Global and European climate impacts of a slow-  
 370 down of the AMOC in a high resolution GCM. *Climate Dynamics*, *45*(11),  
 371 3299–3316. Retrieved from <https://doi.org/10.1007/s00382-015-2540-2>  
 372 doi: 10.1007/s00382-015-2540-2
- 373 Lenton, T. M., Held, H., Kriegler, E., Hall, J. W., Lucht, W., Rahmstorf, S., &  
 374 Schellnhuber, H. J. (2008). Tipping elements in the Earth’s climate system.  
 375 *Proceedings of the National Academy of Sciences*, *105*(6), 1786–1793. Re-  
 376 trieved from <https://www.pnas.org/doi/abs/10.1073/pnas.0705414105>  
 377 doi: 10.1073/pnas.0705414105
- 378 Lueker, T. J., Dickson, A. G., & Keeling, C. D. (2000). Ocean pCO<sub>2</sub> calculated  
 379 from dissolved inorganic carbon, alkalinity, and equations for K<sub>1</sub> and K<sub>2</sub>:  
 validation based on laboratory measurements of CO<sub>2</sub> in gas and seawater at

- 380 equilibrium. *Marine Chemistry*, 70(1), 105–119. Retrieved from [https://](https://www.sciencedirect.com/science/article/pii/S0304420300000220)  
 381 [www.sciencedirect.com/science/article/pii/S0304420300000220](https://www.sciencedirect.com/science/article/pii/S0304420300000220) doi:  
 382 [https://doi.org/10.1016/S0304-4203\(00\)00022-0](https://doi.org/10.1016/S0304-4203(00)00022-0)
- 383 Lynch-Stieglitz, J. (2017). The Atlantic Meridional Overturning Circulation and  
 384 Abrupt Climate Change. *Annual Review of Marine Science*, 9(1), 83–104.  
 385 Retrieved from <https://doi.org/10.1146/annurev-marine-010816-060415>  
 386 doi: 10.1146/annurev-marine-010816-060415
- 387 Marchal, O., Stocker, T. F., & Joos, F. (1998, jun). Impact of oceanic reorganiza-  
 388 tions on the ocean carbon cycle and atmospheric carbon dioxide content. *Pa-*  
 389 *leoceanography*, 13(3), 225–244. Retrieved from [https://doi.org/10.1029/](https://doi.org/10.1029/98PA00726)  
 390 [98PA00726](https://doi.org/10.1029/98PA00726) doi: <https://doi.org/10.1029/98PA00726>
- 391 Matsumoto, K., & Yokoyama, Y. (2013, jun). Atmospheric  $\Delta^{14}\text{C}$  reduction in  
 392 simulations of Atlantic overturning circulation shutdown. *Global Biogeochem-*  
 393 *ical Cycles*, 27(2), 296–304. Retrieved from [https://doi.org/10.1002/](https://doi.org/10.1002/gbc.20035)  
 394 [gbc.20035](https://doi.org/10.1002/gbc.20035) doi: <https://doi.org/10.1002/gbc.20035>
- 395 McKay, D. I. A., Staal, A., Abrams, J. F., Winkelmann, R., Sakschewski, B., Lo-  
 396 riani, S., ... Lenton, T. M. (2022). Exceeding 1.5°C global warm-  
 397 ing could trigger multiple climate tipping points. *Science*, 377(6611),  
 398 eabn7950. Retrieved from [https://www.science.org/doi/abs/10.1126/](https://www.science.org/doi/abs/10.1126/science.abn7950)  
 399 [science.abn7950](https://www.science.org/doi/abs/10.1126/science.abn7950) doi: 10.1126/science.abn7950
- 400 Millero, F. J. (1983). CHAPTER 43 - Influence of Pressure on Chemical Pro-  
 401 cesses in the Sea. In J. P. RILEY & R. B. T. C. O. CHESTER (Eds.), (pp.  
 402 1–88). Academic Press. Retrieved from [https://www.sciencedirect.com/](https://www.sciencedirect.com/science/article/pii/B9780125886086500079)  
 403 [science/article/pii/B9780125886086500079](https://www.sciencedirect.com/science/article/pii/B9780125886086500079) doi: [https://doi.org/10.1016/](https://doi.org/10.1016/B978-0-12-588608-6.50007-9)  
 404 [B978-0-12-588608-6.50007-9](https://doi.org/10.1016/B978-0-12-588608-6.50007-9)
- 405 Mucci, A. (1983, sep). The solubility of calcite and aragonite in seawater at various  
 406 salinities, temperatures, and one atmosphere total pressure. *American Journal*  
 407 *of Science*, 283, 780–799. Retrieved from [https://ui.adsabs.harvard.edu/](https://ui.adsabs.harvard.edu/abs/1983AmJS..283..780M)  
 408 [abs/1983AmJS..283..780M](https://ui.adsabs.harvard.edu/abs/1983AmJS..283..780M) doi: 10.2475/ajs.283.7.780
- 409 Munhoven, G. (2013). Mathematics of the total alkalinity–pH equation - path-  
 410 way to robust and universal solution algorithms: the SolveSAPHE pack-  
 411 age v1.0.1. *Geoscientific Model Development*, 6(4), 1367–1388. Retrieved  
 412 from <https://gmd.copernicus.org/articles/6/1367/2013/> doi:  
 413 [10.5194/gmd-6-1367-2013](https://doi.org/10.5194/gmd-6-1367-2013)
- 414 O'Neill, C. M., Hogg, A. M., Ellwood, M. J., Eggins, S. M., & Opdyke, B. N. (2019).  
 415 The [simple carbon project] model v1.0. *Geoscientific Model Development*,  
 416 12(4), 1541–1572. Retrieved from [https://gmd.copernicus.org/articles/](https://gmd.copernicus.org/articles/12/1541/2019/)  
 417 [12/1541/2019/](https://gmd.copernicus.org/articles/12/1541/2019/) doi: 10.5194/gmd-12-1541-2019
- 418 Palter, J. B. (2015). The Role of the Gulf Stream in European Climate. *Annual Re-*  
 419 *view of Marine Science*, 7(1), 113–137. Retrieved from [https://doi.org/10](https://doi.org/10.1146/annurev-marine-010814-015656)  
 420 [.1146/annurev-marine-010814-015656](https://doi.org/10.1146/annurev-marine-010814-015656) doi: 10.1146/annurev-marine-010814-  
 421 -015656
- 422 Rahmstorf, S. (2002). Ocean circulation and climate during the past 120,000 years.  
 423 *Nature*, 419(6903), 207–214. Retrieved from [https://doi.org/10.1038/](https://doi.org/10.1038/nature01090)  
 424 [nature01090](https://doi.org/10.1038/nature01090) doi: 10.1038/nature01090
- 425 Schmittner, A., & Galbraith, E. D. (2008). Glacial greenhouse-gas fluctuations con-  
 426 trolled by ocean circulation changes. *Nature*, 456(7220), 373–376. Retrieved  
 427 from <https://doi.org/10.1038/nature07531> doi: 10.1038/nature07531
- 428 Sinet, S., von der Heydt, A. S., & Dijkstra, H. A. (2023, jan). AMOC Stabilization  
 429 Under the Interaction With Tipping Polar Ice Sheets. *Geophysical Research*  
 430 *Letters*, 50(2), e2022GL100305. Retrieved from [https://doi.org/10.1029/](https://doi.org/10.1029/2022GL100305)  
 431 [2022GL100305](https://doi.org/10.1029/2022GL100305) doi: <https://doi.org/10.1029/2022GL100305>
- 432 Sun, Y., Knorr, G., Zhang, X., Tarasov, L., Barker, S., Werner, M., & Lohmann, G.  
 433 (2022). Ice sheet decline and rising atmospheric CO<sub>2</sub> control AMOC sensitivity  
 434 to deglacial meltwater discharge. *Global and Planetary Change*, 210, 103755.

- 435 Retrieved from <https://www.sciencedirect.com/science/article/pii/S0921818122000224> doi: <https://doi.org/10.1016/j.gloplacha.2022.103755>
- 436
- 437 van der Ploeg, R., Cramwinckel, M. J., Kocken, I. J., Leutert, T. J., Bohaty, S. M.,
- 438 Fokkema, C. D., ... Sluijs, A. (2023). North Atlantic surface ocean warming
- 439 and salinization in response to middle Eocene greenhouse warming. *Science*
- 440 *Advances*, 9(4), eabq0110. Retrieved from <https://www.science.org/doi/abs/10.1126/sciadv.abq0110> doi: 10.1126/sciadv.abq0110
- 441
- 442 Vellinga, M., & Wood, R. A. (2002). Global Climatic Impacts of a Collapse of the
- 443 Atlantic Thermohaline Circulation. *Climatic Change*, 54(3), 251–267. Re-
- 444 trieved from <https://doi.org/10.1023/A:1016168827653> doi: 10.1023/A:
- 445 1016168827653
- 446 Vellinga, M., & Wood, R. A. (2008). Impacts of thermohaline circulation
- 447 shutdown in the twenty-first century. *Climatic Change*, 91(1), 43–63.
- 448 Retrieved from <https://doi.org/10.1007/s10584-006-9146-y> doi:
- 449 10.1007/s10584-006-9146-y
- 450 Weijer, W., Cheng, W., Drijfhout, S. S., Fedorov, A. V., Hu, A., Jackson, L. C., ...
- 451 Zhang, J. (2019, aug). Stability of the Atlantic Meridional Overturning Cir-
- 452 culation: A Review and Synthesis. *Journal of Geophysical Research: Oceans*,
- 453 124(8), 5336–5375. Retrieved from <https://doi.org/10.1029/2019JC015083>
- 454 doi: <https://doi.org/10.1029/2019JC015083>
- 455 Weijer, W., Cheng, W., Garuba, O. A., Hu, A., & Nadiga, B. T. (2020, jun).
- 456 CMIP6 Models Predict Significant 21st Century Decline of the Atlantic
- 457 Meridional Overturning Circulation. *Geophysical Research Letters*, 47(12),
- 458 e2019GL086075. Retrieved from <https://doi.org/10.1029/2019GL086075>
- 459 doi: <https://doi.org/10.1029/2019GL086075>
- 460 Weiss, R. F. (1974). Carbon dioxide in water and seawater: the solubility
- 461 of a non-ideal gas. *Marine Chemistry*, 2(3), 203–215. Retrieved from
- 462 <https://www.sciencedirect.com/science/article/pii/0304420374900152>
- 463 doi: [https://doi.org/10.1016/0304-4203\(74\)90015-2](https://doi.org/10.1016/0304-4203(74)90015-2)
- 464 Williams, R. G., & Follows, M. J. (2011). *Ocean Dynamics and the Carbon Cycle: Principles and Mechanisms*. Cambridge: Cambridge University Press. Re-
- 465 trieved from [https://www.cambridge.org/core/books/ocean-dynamics](https://www.cambridge.org/core/books/ocean-dynamics-and-the-carbon-cycle/31EF28FEF48A172FF746B3E654F9455A)
- 466 [-and-the-carbon-cycle/31EF28FEF48A172FF746B3E654F9455A](https://www.cambridge.org/core/books/ocean-dynamics-and-the-carbon-cycle/31EF28FEF48A172FF746B3E654F9455A) doi:
- 467 DOI:10.1017/CBO9780511977817
- 468
- 469 Wunderling, N., Donges, J. F., Kurths, J., & Winkelmann, R. (2021). In-
- 470 teracting tipping elements increase risk of climate domino effects under
- 471 global warming. *Earth System Dynamics*, 12(2), 601–619. Retrieved
- 472 from <https://esd.copernicus.org/articles/12/601/2021/> doi:
- 473 10.5194/esd-12-601-2021
- 474 Zeebe, R. E., Zachos, J. C., & Dickens, G. R. (2009). Carbon dioxide forcing alone
- 475 insufficient to explain Palaeocene–Eocene Thermal Maximum warming. *Nature Geoscience*, 2(8), 576–580. Retrieved from <https://doi.org/10.1038/ngeo578> doi: 10.1038/ngeo578
- 476
- 477
- 478 Zhang, X., Knorr, G., Lohmann, G., & Barker, S. (2017). Abrupt North At-
- 479 lantic circulation changes in response to gradual CO<sub>2</sub> forcing in a glacial
- 480 climate state. *Nature Geoscience*, 10(7), 518–523. Retrieved from
- 481 <https://doi.org/10.1038/ngeo2974> doi: 10.1038/ngeo2974

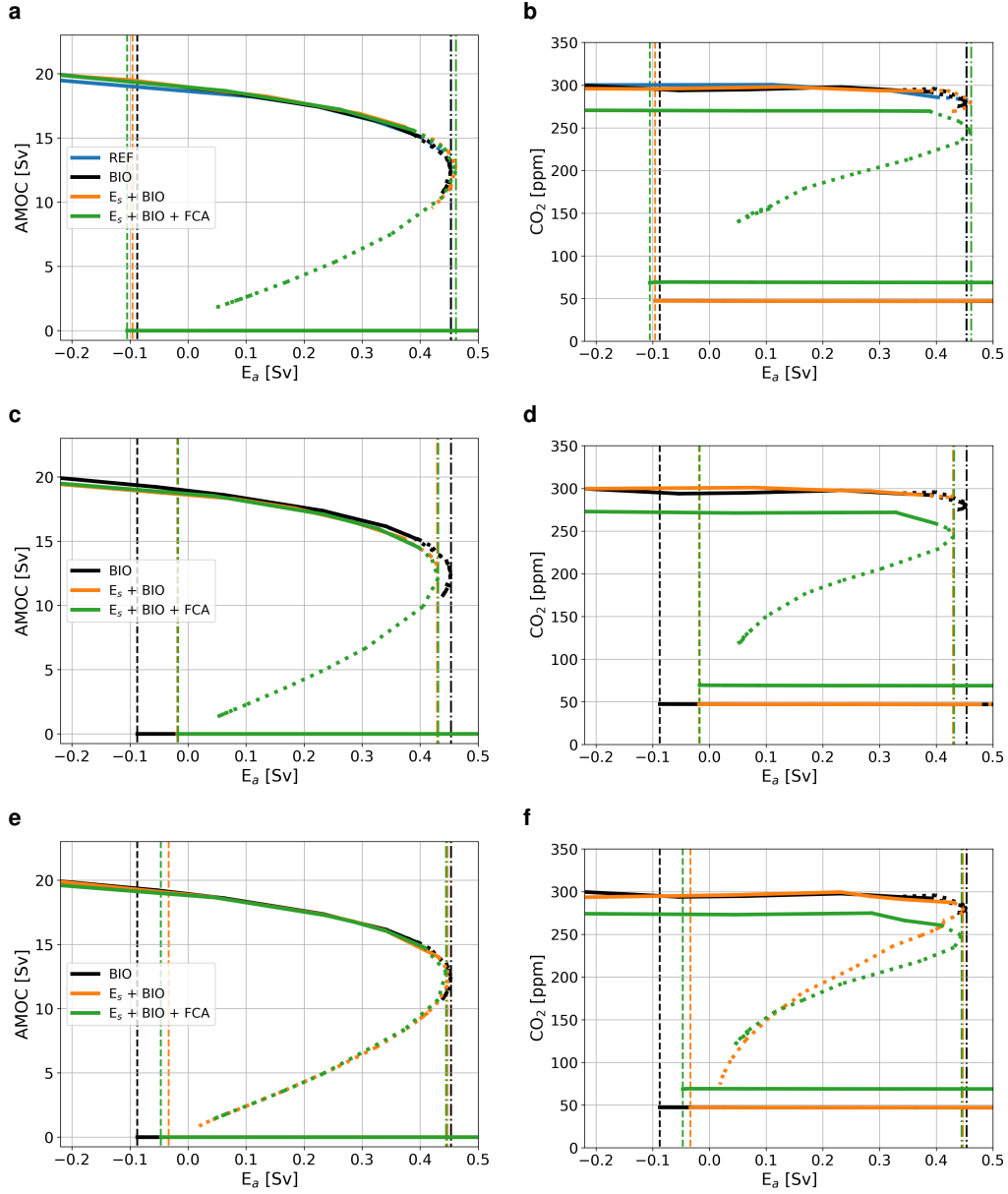


**Figure 2.** Bifurcation diagram showing the sensitivity of the AMOC to  $E_a$ . Solid lines represent stable steady state solutions, dotted lines represent unstable solutions, dash-dotted lines represent the location of the saddle node on the on-branch, and dashed lines the location of the saddle node on the off-branch. The blue lines represent a case without biological,  $E_s$ - $pCO_2$  and rain ratio coupling (REF), the black lines with only the biological coupling (BIO), the orange lines with the linear CMIP6 based  $E_s$  and biological coupling ( $E_s + BIO$ ), and the green lines represent a case where also the rain ratio feedback is applied ( $E_s + BIO + FCA$ ). Results are for the AMOC strength in Sv (a) and atmospheric  $pCO_2$  in ppm (b). Case REF is difficult to see in A because it is similar to case BIO except that it does not simulate an off-branch. Panels a and b are for Eq. 1, panels c and d are for Eq. 2 and panels e and f are for Eq. 3. In a, b, c and d the orange saddle node lines are located behind the green lines.

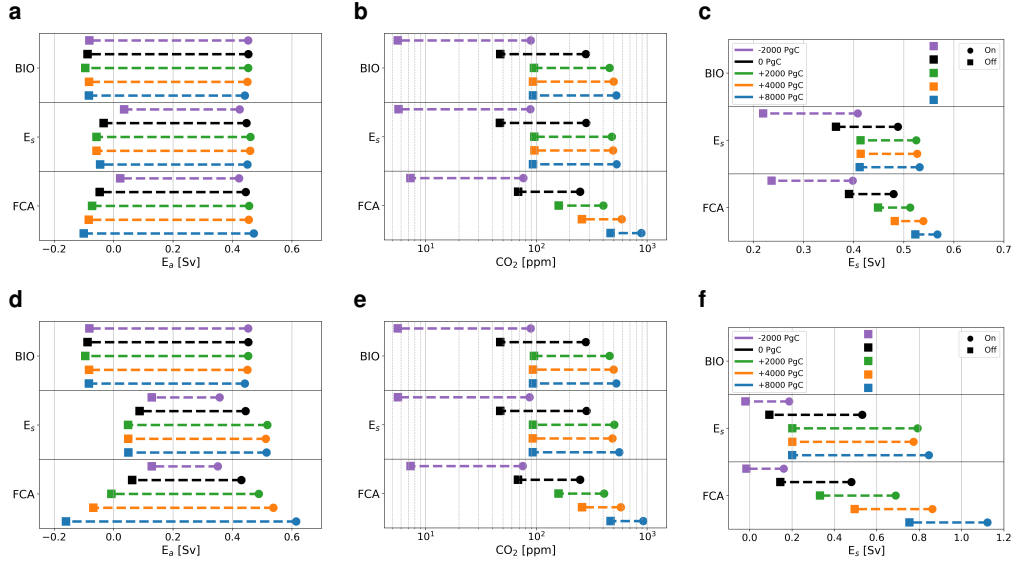


**Figure 3.** Panel a shows the location of the saddle nodes versus  $E_a$  in Sv, panel b shows the corresponding  $\text{CO}_2$  concentration in ppm (note that the x-axis is logarithmic), and c shows the corresponding value of  $E_s$  in Sv following Eq. 2. In A-C the top of the figure represents case BIO, the middle case  $E_s + \text{BIO}$ , and the bottom case  $E_s + \text{BIO} + \text{FCA}$ . Square markers represent the location of the saddle node on the off-branch and round markers the location of the saddle node on the on-branch for cases where 4000 PgC is removed (purple), 2000 PgC is removed (black), the default carbon content (green), 4000 PgC is added (orange) and where 8000 PgC is added (blue) to the the standard case considered in Fig. 2. Panels d-f are as in a-c but for the  $E_s$  coupling in Eq. 3.

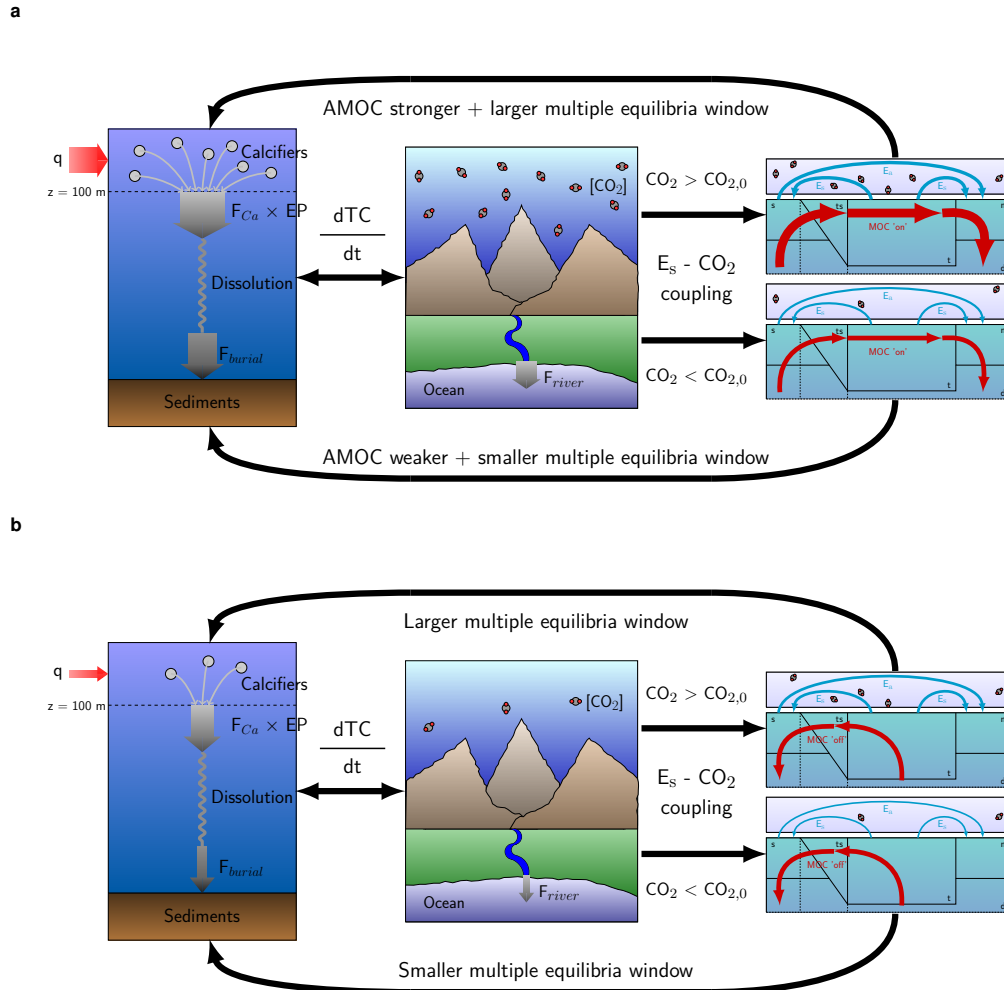


**Figure 4.** Illustrations of the main mechanisms affecting atmospheric  $p\text{CO}_2$  and AMOC stability. Panel a shows the mechanisms for the on-branch. A strong AMOC increases export production through increased nutrient advection (left panel), which is accompanied by a high atmospheric  $p\text{CO}_2$  due to the necessary balance between the river influx and sediment burial (middle panel). If the  $\text{CO}_2$  concentration is larger (smaller) than  $\text{CO}_{2,0}$  than the AMOC will strengthen (weaken) and the MEW increases (decreases) (right panels). Panel b shows the mechanisms for the off-branch. The absence of an AMOC decreases export production through decreased nutrient advection (left panel), accompanied by a low atmospheric  $p\text{CO}_2$  (middle panel). When  $p\text{CO}_2$  is larger (smaller) than  $p\text{CO}_{2,0}$  the MEW increases (decreases) (right panel).

# Supporting Information for Potential effect of the marine carbon cycle on the multiple equilibria window of the Atlantic Meridional Overturning Circulation”

A. Boot<sup>1</sup>, A. S. Von der Heydt<sup>1,2</sup>, and H. A. Dijkstra<sup>1,2</sup>

<sup>1</sup>Institute for Marine and Atmospheric research Utrecht, Department of Physics, Utrecht University, Utrecht, the Netherlands

<sup>2</sup>Center for Complex Systems Studies, Utrecht University, Utrecht, the Netherlands

## Contents of this file

1. The ocean circulation box model description
2. The carbon cycle box model description
3. Couplings and feedbacks in the model
4. Model equations
5. Solution method
6. Table S1-S7
7. Figure S1-S3

**Introduction** The supplementary information includes a more extensive description of both the ocean circulation and the carbon cycle box model, the way they are coupled and

---

how the model equations are solved. Supplementary tables are given with information about the considered cases, and the parameter values. Supplementary figures include the CMIP6 fits, additional cases, and the model sensitivity to  $E_s$ .

### **The ocean circulation box model**

The box model representing the dynamics of the AMOC simulates the depth of the pycnocline and the distribution of salt in the Atlantic Ocean and the Southern Ocean. It consists of 5 boxes, and therefore 6 prognostic variables. The northern box  $n$  represents the regions of deep water formation in the North Atlantic and box  $s$  represents the entire Southern Ocean (i.e. all longitudes). There are two thermocline boxes  $t$  and  $ts$  where box  $ts$  represents the region between  $30^\circ\text{S}$  and  $40^\circ\text{S}$  which is characterized by strong sloping isopycnals where the pycnocline becomes shallower moving poleward. Underneath the four surface boxes, there is one box ( $d$ ) representing the deep ocean.

The distribution of salinity in the model is dependent on the ocean circulation and freshwater fluxes. There are multiple volume fluxes in the model. In the Southern Ocean, there is wind-induced Ekman transport into the Atlantic ( $q_{Ek}$ ), and there is an eddy induced transport from the Atlantic into the Southern Ocean ( $q_e$ ) which is dependent on the pycnocline depth  $D$ . The difference between the two, defined as  $q_S$ , represents upwelling in the Southern Ocean and net volume transport into the Atlantic thermocline. The thermocline also is sourced with water from box  $d$  through diffusive upwelling ( $q_U$ ). The strength of the downward branch of the AMOC is represented in the North Atlantic by  $q_N$ . This downwelling is dependent on the meridional density gradient between box  $ts$  and box  $n$ , where the density is determined using a linear equation of state. Wind driven

gyre transport is modelled by  $r_N$  in the Northern Hemisphere, and  $r_S$  in the Southern Hemisphere. Salinity is also affected by two surface freshwater fluxes, modelled as virtual salt fluxes. First, there is a symmetrical forcing  $E_s$ , i.e. the freshwater flux is the same for both hemispheres; and secondly, there is an asymmetrical forcing  $E_a$  which results in interhemispheric differences. This last parameter can be viewed as a hosing parameter for the AMOC strength since it regulates the salinity of box n. The pycnocline depth is an important state variable in this model since several volume fluxes are dependent on it. This depth is dependent on four different volume fluxes going in and out of the two thermocline boxes t and ts ( $q_e, q_{Ek}, q_U, q_N$ ).

The model provides a simple framework to study AMOC dynamics and has already been used to show both slow (Cimatoribus et al., 2014) and fast, noise-induced (Castellana et al., 2019) tipping of the AMOC by freshwater forcing. However, several assumptions are made. The most important assumptions are that we neglect diapycnal mixing, and that temperature anomalies do not affect the AMOC strength (i.e. temperature is not a prognostic variable), since temperature anomalies have a faster decay timescales compared to salinity anomalies. Compared to earlier versions of the model we will use a different default value for  $E_s$ . In previous studies values of 0.25Sv (Cimatoribus et al., 2014) and 0.17Sv (Castellana et al., 2019) have been used. Here we choose a default value of 0.56Sv based on the CMIP6 multi model mean value at a CO<sub>2</sub> concentration of 300 ppm.

Satellite based observations of the HOAPS4.0 data (Andersson et al., 2017) show a net freshwater flux of 1 Sv averaged over the period 1987-2015 into the region representing the thermocline box. This results in an  $E_s$  value of 0.5Sv and therefore close to the chosen default value based on the CMIP6 ensemble. Basing the default value on the CMIP6 ensemble, instead of on observations, is done to enable use to easier compare the reference cases with cases where the CMIP6 fitted  $E_s$  (Eq. 1 and Eq. 2 in the main text) coupling is used. Since observational values are close to the CMIP6 multi model mean value, we consider the model to give an adequate representation of the Atlantic Ocean.

### **The carbon cycle box model**

The carbon cycle model is based on the equations of the SCP-M (O'Neill et al., 2019). The original SCP-M has two terrestrial carbon stocks, an atmosphere box, and 7 ocean boxes representing the global ocean. In the ocean multiple tracers are simulated that are important for the marine carbon cycle. In this study, we do not use the terrestrial biosphere and we have adapted the box structure to represent the box structure of the ocean circulation model, which only represents the Atlantic Ocean and the Southern Ocean. Some assumptions had to be made here. First of all, the depth of boxes n and s is not given in Cimadoribus et al. (2014) but is necessary for the carbon cycle model. We assume these to be 300 m. The total depth of the ocean is assumed to be 4000 m. Secondly, the riverine fluxes in the SCP-M represent the entire global riverine input, while the circulation model only simulates a part of the global domain. We use a volume fraction (volume circulation model / volume SCP-M = 0.2) to scale the river fluxes.

Another adaption we have made is that we only use three tracers: dissolved inorganic carbon (DIC), alkalinity (Alk), and phosphate ( $\text{PO}_4$ ). All tracers are affected by the dynamical circulation simulated in the ocean circulation model in a similar fashion as salinity. DIC is affected by biological production and remineralization (soft tissue pump), the formation and dissolution of calcium carbonate ( $\text{CaCO}_3$ ; carbonate pump), and gas exchange with the atmosphere. Alk is only affected by the carbonate pump, and  $\text{PO}_4$  only by the soft tissue pump. All three tracers have a riverine source flowing into box  $t$  and a sink to the sediments.  $\text{PO}_4$  is explicitly conserved in the system, i.e. the source of  $\text{PO}_4$  is equal to the sink of  $\text{PO}_4$  at all times. DIC and Alk, however, can vary since the time dependent riverine influx is not necessarily equal to the sediment outflux. The change in total carbon (DIC + atmospheric  $\text{CO}_2$ ) and Alk in the atmosphere-ocean system can be captured in two ODEs as the sum of riverine influx and the sediment outflux. The riverine influx is a function of atmospheric  $\text{pCO}_2$  and represents the weathering of silicate and carbonate rocks i.e.,

$$C_{river} = W_{carb,c} + (W_{carb,v} + W_{si}) \times CO_2^{atm} \quad (1)$$

The sediment outflux of DIC is determined by the sum of the soft tissue and the carbonate pumps over the entire ocean. In this model, generally all produced organic matter is also remineralized, causing the contribution of the soft tissue pump to be negligible resulting in

$$C_{sed} = C_{river} \times V_t + \sum_{i=1}^5 (C_{carb,i} \times V_i) \quad (2)$$

Without the influence of the soft tissue pump, the change in total carbon and total Alk are proportional, where the change in total Alk is twice as big as the change in total carbon. For the dissolution of  $\text{CaCO}_3$  and the gas exchange of carbon, the pH needs to be determined. In the original SCP-M a simple function is used where the pH of timestep  $i-1$  is used as an initial guess for timestep  $i$  (Follows et al., 2006). As long as the changes per time step remain relatively small, this scheme is sufficiently accurate. However, due to our solution method, in which steady states are calculated versus parameters, this function is not suitable for this study. Therefore, we have chosen a simple ‘text-book’ carbonate chemistry (Williams & Follows, 2011; Munhoven, 2013) where Alk is assumed to be equal to carbonate alkalinity ( $\text{Alk}_{carb} = [\text{HCO}_3^-] + [\text{CO}_3^{2-}]$ ). This method is less accurate and leads to higher pH values (Munhoven, 2013) and lower atmospheric  $\text{pCO}_2$  values (Boot et al., 2022). Since we use a different carbonate chemistry, the atmospheric  $\text{pCO}_2$  values are relatively low. Furthermore, the model used in Boot et al. (2022) is tuned globally whereas here we only take the Atlantic and Southern Ocean into account. We therefore retune the model in order to approach  $\text{CO}_2$  concentrations of around 300 ppm for cases REF and BIO. To accomplish this, we have retuned the export production (general decrease) and rain ratio (increase from 0.07 to 0.15). We have also chosen different values for the biological efficiencies in Eq. 4 below compared to Boot et al. (2022) to get similar atmospheric  $\text{pCO}_2$  values for cases REF and BIO at  $E_a = 0 \text{ Sv}$ .

### **Couplings and feedbacks in the model**

The first coupling between the physical and the carbon cycle model is through the ocean circulation. The AMOC determined in the circulation model is used for the advec-

tive transport of the three tracers in the carbon cycle model providing a first coupling between the two models. We have implemented additional couplings between the model and specific feedbacks within the carbon cycle model. Several of these feedbacks have previously been introduced into the SCP-M (Boot et al., 2022).

As explained earlier, we have introduced a coupling between  $E_s$  and atmospheric  $p\text{CO}_2$  (Eq. 1 and 2 in the main text; Fig. S1b). These are simple linear and logarithmic functions based on a fit to a CMIP6 multi-model mean forced under the 1%  $\text{CO}_2$  increase scenario (Eyring et al., 2016). We have used 28 different models to determine the multi-model mean (Fig. S1a). A list of the used models and the references for the data can be found in a separate data sheet. We have used all models available, except for a few for which we had difficulty downloading the model data. Each model was first regridded to a rectilinear grid, then we integrated the freshwater flux over the region that represents the thermocline box of the box model and  $E_s$  was determined dividing this number by 2. After this, all models and the multi-model mean were smoothed with a 5-year moving mean. The regions used in the CMIP6 model are for box t the Atlantic Ocean between  $50^\circ\text{N}$  and  $30^\circ\text{S}$ . The fits represent a feedback that the subtropical ocean becomes drier while the subpolar regions in both the northern and the southern hemisphere become wetter under  $\text{CO}_2$  forcing. This coupling is the only way how the carbon cycle model can influence the circulation model. Both fits are used in Section 3.1 of the main text since the fits have different behavior for  $p\text{CO}_2$  values below 300 ppm. Also a different logarithmic coupling is used (Eq. 3 in the main text; Fig. S1c) to test the sensitivity to

different  $E_s$ -pCO<sub>2</sub> coupling strengths. This fit, is used in Section 3.1 and together with Eq. 2 also in Section 3.2.

The other two couplings are a one way coupling from the circulation model to the carbon cycle model. First, we introduce dilution fluxes to both DIC and Alk coupled to the freshwater fluxes  $E_s$  and  $E_a$  (Eq. 3). Increasing the concentrations of DIC and Alk due to evaporation and decreasing the concentrations due to a net influx of freshwater at the surface. Lastly, we create a dependency of the biological export production in the surface boxes to the amount of PO<sub>4</sub> advected into the specific surface box and therefore introducing a dependency on the ocean circulation (see below).

$$C_{dil,i} = \lambda_D \times (E_s + E_a) \times \frac{C_i}{V_i} \quad (3)$$

Where  $C_i$  is the tracer concentration in box  $i$  and  $V_i$  the volume, and  $\lambda_D$  is a parameter that determines whether the coupling is used ( $\lambda_D = 1$ ) or not ( $\lambda_D = 0$ ).

$$Z_i = (1 - \lambda_{BI}) \times Z_{i,base} + \lambda_{BI} \times (q_{j \rightarrow i} \times [PO_4^{3-}]_j + P_{river,t}) \times \epsilon_i \quad (4)$$

Here  $Z$  represents the export production,  $\lambda_{BI}$  a parameter to switch between the default value of  $Z$  ( $Z_{i,base}$ ;  $\lambda_{BI} = 0$ ) and the variable export production ( $\lambda_{BI} = 1$ ). In addition,  $q$  represents the volume transport,  $P_{river}$  the riverine influx of PO<sub>4</sub> in box  $t$ , and  $\epsilon_i$  represents a biological efficiency term.

Besides coupling the models, we also introduce (non-linear) feedbacks in the carbon cycle model. First of all, we allow the sea surface temperatures (SSTs) to vary with

atmospheric pCO<sub>2</sub> following a logarithmic function and a climate sensitivity parameter (Eq. 5 and 6):

$$T_i = T_{i,base} + \Delta T_i \quad (5)$$

$$\Delta T_i = \lambda_T \times 0.54 \text{ times } 5.35 \ln\left(\frac{CO_2}{CO_{2,0}}\right) \quad (6)$$

By varying the parameter  $\lambda_T$  we are able to change the climate sensitivity of the model. Changing the SSTs will also change the density in the ocean circulation model. However, since we use a linear equation of state and the change of SST is homogeneous over all boxes, it does not influence the dynamical ocean circulation and is therefore not a coupling but a feedback within the carbon cycle.

A second feedback we introduce is a linear temperature dependency in the biological efficiency which was introduced in the biological coupling (Eq. 7). Under an SST increase, the efficiency will decrease following

$$\epsilon_i = (\lambda_\epsilon \times -0.1\Delta T) + \epsilon_{i,base} \quad (7)$$

For this feedback it is necessary to also use the temperature feedback and the strength can be regulated with  $\lambda_{\epsilon}$ .

The third feedback allows the piston velocity ( $k_w$ ) to vary with the SSTs (Eq. 8). When the SST feedback is used, this also affects the piston velocity. The temperature dependency is introduced by making the piston velocity a function of the Schmidt number

(Eq. 9) following

$$k_{w,i} = (1 - \lambda_P) \times k_{w,ibase} + \lambda_P k_{w,ibase} \times \left(\frac{Sc_i}{660}\right)^{-0.5} \quad (8)$$

Where

$$Sc_i = 2116.8 - 136.25T_i + 4.7353T_i^2 - 0.092307T_i^3 + 0.0007555T_i^4 \quad (9)$$

In this case the feedback can either be switched on ( $\lambda_P = 1$ ) or off ( $\lambda_P = 0$ ). Without this feedback the piston velocity is similar for all boxes, but with this feedback the piston velocity will differ per box. Lastly, we have introduced a feedback on the rain ratio (Eq. 10) making it dependent on the saturation state of  $\text{CaCO}_3$  following

$$F_{Ca,i} = (1 - \lambda_F) \times F_{Ca,base} + \lambda_F \times 0.022 \left(\frac{[Ca_i^{2+}][CO_3^{2-}]}{K_{sp,i}}\right)^{0.81} \quad (10)$$

Similar as for the piston velocity  $\lambda_F$  is either 0 or 1, and including this feedback will introduce different rain ratios per box. In the main text only cases using the biological coupling (BIO), the  $E_s$ -coupling ( $E_s$ ) and the rain ratio (FCA) have been shown. In the supplementary material more simulations, also using the couplings and feedbacks described above, are shown.

**Model equations** There are in total 21 state variables: salinity, DIC, alkalinity, and  $\text{PO}_4$  in the 5 boxes, and the pycnocline depth  $D$ . The state variables in the deep box are determined using conservation laws. The salinity equations are given by Eq. 12-15, the pycnocline depth is determined using Eq. 16.

$$\frac{d(V_t S_t)}{dt} = q_S(\theta(q_S)S_{ts} + \theta(-q_S)S_t + q_U S_d - \theta(q_N)q_N S_t + r_s(S_{ts} - S_t) + r_N(S_n - S_t) + 2E_s S_0 \quad (11)$$

$$\frac{d(V_{ts}S_{ts})}{dt} = q_{Ek}S_s - q_eS_{ts} - q_S(\theta(q_S)S_{ts} + \theta(-q_S)S_t) + r_S(S_t - S_{ts}) \quad (12)$$

$$V_n \frac{dS_n}{dt} = \theta(q_N)q_N(S_t - S_n) + r_N(S_t - S_n) - (E_s + E_a)S_0 \quad (13)$$

$$V_s \frac{dS_s}{dt} = q_S(\theta(q_S)S_d + \theta(-q_S)S_s) + q_eS_{ts} - q_{Ek}S_s - (E_s - E_a)S_0 \quad (14)$$

$$\left(A + \frac{L_{xA}L_y}{2}\right) \frac{dD}{dt} = q_U + q_{Ek} - q_e - \theta(q_N)q_N \quad (15)$$

$$S_0V_0 = V_nS_n + V_dS_d + V_tS_t + V_{ts}S_{ts} + V_sS_s \quad (16)$$

Where:

$$q_{Ek} = \frac{\tau L_{xS}}{\rho_0 |f_S|} \quad (17)$$

$$q_e = A_{GM} \frac{L_{xA}}{L_y} D \quad (18)$$

$$q_U = \frac{\kappa A}{D} \quad (19)$$

$$q_N = \eta \frac{\rho_n - \rho_{ts}}{\rho_0} D^2 \quad (20)$$

$$q_S = q_{Ek} - q_e \quad (21)$$

$$\rho_i = \rho_0(1 - \alpha(T_i - T_0) + \beta(S_i - S_0)) \quad (22)$$

$$\frac{d[DIC]_i}{dt} = C_{phys,i} + C_{bio,i} + C_{carb,i} + C_{air,i} + C_{river,t} \quad (23)$$

$$\frac{d[Alk]_i}{dt} = A_{phys,i} + A_{carb,i} + A_{river,t} \quad (24)$$

$$\frac{d[PO_4^{3-}]_i}{dt} = P_{phys,i} + P_{bio,i} + P_{river,t} \quad (25)$$

$$\frac{dC_{tot}}{dt} = C_{river,t} \times V_t + \sum_{i=1}^5 (C_{carb,i} V_i) + \sum_{i=1}^5 (C_{bio,i} V_i) \quad (26)$$

In these equations the different terms represent advective fluxes ( $X_{phys}$ ), biological fluxes ( $X_{bio}$ ), carbonate fluxes ( $X_{carb}$ ), air-sea gas exchange ( $C_{air}$ ) and the river influx ( $X_{river}$ ), which are determined following:

$$X_{phys,i} = \frac{1}{V_i} \left( \sum_{j=1}^5 (q_{j \rightarrow i} \times X_j) - \sum_{j=1}^5 (q_{i \rightarrow j} \times X_i) \right) \quad (27)$$

This equation represents that the concentration  $X$  changes through an advective flux flowing out of box  $i$  to box  $j$  ( $q_{i \rightarrow j}$  times the concentration in box  $i$  ( $X_i$ ), and a flux flowing

into box  $i$  from box  $j$  ( $q_{j \rightarrow i}$ ) times the concentration in box  $j$  ( $X_j$ ). There can be fluxes from multiple boxes into one box.

$$C_{air,i} = \frac{K_{0,i} \times k_{w,i} \times \rho_0 \times (CO_2^{atm} - pCO_{2,i})}{V_i} \quad (28)$$

For  $i$  is n, t, ts or s.  $K_0$  is the solubility constant,  $k_w$  the piston velocity,  $CO_2^{atm}$  the atmospheric  $CO_2$  concentration,  $pCO_2$  the partial pressure of  $CO_2$  in the ocean and  $V$  the volume of the ocean box.

$$C_{carb,i} = -\frac{Z_i t \times A_i C_{a,i}}{V_i} + ([CO_3^{2-}]_i [Ca^{2+}]_i) \rho_0 k_{Ca} \left(1 - \frac{([CO_3^{2-}]_i [Ca^{2+}]_i)}{K_{sp,i}}\right)^n \times PerC + DC \quad (29)$$

For  $i$  is n, t, ts, or s.  $Z$  represent biological production,  $A$  the surface area of the box,  $F_{Ca}$  the rain ratio and  $V$  the volume. Other variables are the carbonate ion concentration ( $[CO_3^{2-}]$ ), calcium concentration ( $[Ca^{2+}]$ ), and equilibrium constant for  $CaCO_3$  dissolution ( $K_{sp}$ ).

$$C_{bio,i} = \frac{Z_i \times A_i}{V_i} \times \left(\frac{d_{fi}}{d_0}\right)^{-b} \quad (30)$$

For  $i$  is n, t, ts or s.  $Z$  represent biological production,  $A$  the surface area of the box,  $V$  the volume, and  $d_{fi}$  the floor depth of the box.

$$A_{carb,i} = 2 \times C_{carb,i} \quad (31)$$

$$P_{bio,i} = r_{P:C} \times C_{bio,i} \quad (32)$$

An explanation and the value of all parameters are given in the tables in this document.

### The solution method

Our coupled system is a system of 22 ODEs (four tracers per box, the pycnocline depth and atmospheric pCO<sub>2</sub>) of the form

$$\frac{d\mathbf{u}}{dt} = f(\mathbf{u}(t), \mathbf{p}) \quad (33)$$

Here  $\mathbf{u}$  is the state vector (containing all the dependent quantities in all boxes),  $f$  contains the right-hand-side of the equations and  $\mathbf{p}$  is the parameter vector. To solve this system of equations we use the continuation software AUTO-07p (Doedel et al., 2007). Both the circulation model (Cimatoribus et al., 2014), and the SCP-M (Boot et al., 2022) have already been implemented in the software before. AUTO enables us to efficiently compute branches of stable and unstable steady state solutions under a varying control parameter. Furthermore, it allows for detection of special points such as saddle-node bifurcations, which is important for determining the multiple equilibria window of the AMOC. However, one of the requirements of AUTO is that the Jacobian of the system is non-singular. To achieve this, we use explicit conservation equations (Eq. 16 and 26) to eliminate the ODEs of the deep box. Both the conservation equation of salt (Eq. 16) and PO<sub>4</sub> are already explicitly included into the model. However, as described previously, this is not the case for DIC and Alk. Therefore, we have to introduce an extra ODE describing the change in total carbon in the system (Eq. 26). Since the change in alkalinity in the

system is proportional to the change in total carbon, only one extra ODE is necessary. By eliminating the ODEs for the deep box and introducing the ODE for total carbon in the ocean-atmosphere system, AUTO can solve the system with 19 ODEs. AUTO has three accuracy parameters. The absolute and relative accuracy differ per specific case, but are set to maximal  $5 \times 10^{-3}$ . The accuracy for the detection of special points (e.g. saddle nodes and Hopf bifurcations) is set to  $10^{-5}$ .

## References

- Andersson, A., Graw, K., Schröder, M., Fennig, K., Liman, J., Bakan, S., ... Klepp, C. (2017). *Hamburg Ocean Atmosphere Parameters and Fluxes from Satellite Data - HOAPS 4.0*. Satellite Application Facility on Climate Monitoring (CM SAF). Retrieved from [https://wui.cmsaf.eu/safira/action/viewDoiDetails?acronym=HOAPS\\\_{ }V002](https://wui.cmsaf.eu/safira/action/viewDoiDetails?acronym=HOAPS\_{ }V002) doi: 10.5676/EUM\_SAF\_CM/HOAPS/V002
- Boot, A., von der Heydt, A. S., & Dijkstra, H. A. (2022). Effect of the Atlantic Meridional Overturning Circulation on atmospheric  $\text{CO}_2$  variations. *Earth System Dynamics*, 13(3), 1041–1058. Retrieved from <https://esd.copernicus.org/articles/13/1041/2022/> doi: 10.5194/esd-13-1041-2022
- Castellana, D., Baars, S., Wubs, F. W., & Dijkstra, H. A. (2019). Transition Probabilities of Noise-induced Transitions of the Atlantic Ocean Circulation. *Scientific Reports*, 9(1), 20284. Retrieved from <https://doi.org/10.1038/s41598-019-56435-6> doi: 10.1038/s41598-019-56435-6
- Cimatoribus, A. A., Drijfhout, S. S., & Dijkstra, H. A. (2014). Meridional overturning circulation: stability and ocean feedbacks in a box model. *Climate Dynamics*, 42(1),

311–328. Retrieved from <https://doi.org/10.1007/s00382-012-1576-9> doi: 10.1007/s00382-012-1576-9

Doedel, E. J., Paffenroth, R. C., Champneys, A. C., Fairgrieve, T. F., Kuznetsov, Y. A., Oldeman, B. E., . . . Wang, X. J. (2007). *AUTO-07p: Continuation and Bifurcation Software for Ordinary Differential Equations*.

Eyring, V., Bony, S., Meehl, G. A., Senior, C. A., Stevens, B., Stouffer, R. J., & Taylor, K. E. (2016, may). Overview of the Coupled Model Intercomparison Project Phase 6 (CMIP6) experimental design and organization. *Geosci. Model Dev.*, *9*(5), 1937–1958. Retrieved from <https://gmd.copernicus.org/articles/9/1937/2016/https://gmd.copernicus.org/articles/9/1937/2016/gmd-9-1937-2016.pdf> doi: 10.5194/gmd-9-1937-2016

Follows, M. J., Ito, T., & Dutkiewicz, S. (2006). On the solution of the carbonate chemistry system in ocean biogeochemistry models. *Ocean Modelling*, *12*(3), 290–301. Retrieved from <http://www.sciencedirect.com/science/article/pii/S1463500305000533> doi: <https://doi.org/10.1016/j.ocemod.2005.05.004>

Lueker, T. J., Dickson, A. G., & Keeling, C. D. (2000). Ocean pCO<sub>2</sub> calculated from dissolved inorganic carbon, alkalinity, and equations for K<sub>1</sub> and K<sub>2</sub>: validation based on laboratory measurements of CO<sub>2</sub> in gas and seawater at equilibrium. *Marine Chemistry*, *70*(1), 105–119. Retrieved from <https://www.sciencedirect.com/science/article/pii/S0304420300000220> doi: [https://doi.org/10.1016/S0304-4203\(00\)00022-0](https://doi.org/10.1016/S0304-4203(00)00022-0)

- Millero, F. J. (1983). CHAPTER 43 - Influence of Pressure on Chemical Processes in the Sea. In J. P. RILEY & R. B. T. C. O. CHESTER (Eds.), (pp. 1–88). Academic Press. Retrieved from <https://www.sciencedirect.com/science/article/pii/B9780125886086500079> doi: <https://doi.org/10.1016/B978-0-12-588608-6.50007-9>
- Mucci, A. (1983, sep). The solubility of calcite and aragonite in seawater at various salinities, temperatures, and one atmosphere total pressure. *American Journal of Science*, 283, 780–799. Retrieved from <https://ui.adsabs.harvard.edu/abs/1983AmJS..283..780M> doi: 10.2475/ajs.283.7.780
- Munhoven, G. (2013). Mathematics of the total alkalinity–pH equation - pathway to robust and universal solution algorithms: the SolveSAPHE package v1.0.1. *Geoscientific Model Development*, 6(4), 1367–1388. Retrieved from <https://gmd.copernicus.org/articles/6/1367/2013/> doi: 10.5194/gmd-6-1367-2013
- O'Neill, C. M., Hogg, A. M., Ellwood, M. J., Eggins, S. M., & Opdyke, B. N. (2019). The [simple carbon project] model v1.0. *Geoscientific Model Development*, 12(4), 1541–1572. Retrieved from <https://gmd.copernicus.org/articles/12/1541/2019/> doi: 10.5194/gmd-12-1541-2019
- Weiss, R. F. (1974). Carbon dioxide in water and seawater: the solubility of a non-ideal gas. *Marine Chemistry*, 2(3), 203–215. Retrieved from <https://www.sciencedirect.com/science/article/pii/0304420374900152> doi: [https://doi.org/10.1016/0304-4203\(74\)90015-2](https://doi.org/10.1016/0304-4203(74)90015-2)
- Williams, R. G., & Follows, M. J. (2011). *Ocean Dynamics and the Carbon Cycle: Principles and Mechanisms*. Cambridge: Cambridge University Press.

Retrieved from <https://www.cambridge.org/core/books/ocean-dynamics-and-the-carbon-cycle/31EF28FEF48A172FF746B3E654F9455A> doi: DOI:10.1017/CBO9780511977817

**Table S1.** Overview of the used cases in the main text. The left column represents the used simulations, where the uncoupled case is added to show the coupling of the carbon cycle in REF. The other columns represent whether a coupling or feedback denoted in the top row is used in the case mentioned in the first column.

Case name	Carbon cycle	BIO	$E_s$	FCA
Uncoupled				
REF	X			
BIO	X	X		
$E_s$ + BIO	X	X	X	
$E_s$ + BIO + FCA	X	X	X	X

**Table S2.** Additional cases not included in the main text using additional feedbacks as described in this document. When the  $E_s$ -coupling is used, the logarithmic CMIP6 fit (Eq. 2 in the main text

is used. Results of these cases can be seen in Figure S2.

Notation	S-1	S-2	S-3	S-4	S-5	S-6	S-7	S-8	S-9	S-10
$\lambda_{BI}$	1	1	1	1	1	1	1	1	1	1
$\lambda_T$	1	0	0	1	1	1	0	0	1	1
$\lambda_P$	0	0	1	1	1	0	0	1	1	1
$\lambda_D$	0	1	0	0	0	0	1	0	0	0
$\lambda_\epsilon$	0	0	0	0	1	0	0	0	0	1
$E_s$	0	0	0	0	0	Eq. 2				

**Table S3.** Symbol (column 1), description (column 2), value (column 3), and units (column 4) of the general parameters used in the ocean circulation model based on Cimatoribus et al. (2014).

Symbol	Description	Value	Units
$V_0$	Total volume of the basin	$3 \times 10^{17}$	$\text{m}^3$
$V_n$	Volume of box n	$3 \times 10^{15}$	$\text{m}^3$
$V_s$	Volume of box s	$9 \times 10^{15}$	$\text{m}^3$
$A_t$	Surface area box t	$1 \times 10^{14}$	$\text{m}^2$
$L_{xA}$	Zonal extent of the Atlantic Ocean at its southern end	$1 \times 10^7$	m
$L_y$	Meridional extent of the frontal region of the Southern Ocean	$1 \times 10^6$	m
$L_{xS}$	Zonal extent of the Southern Ocean	$3 \times 10^7$	m
$\tau$	Average zonal wind stress amplitude	0.1	$\text{N m}^{-2}$
$A_{GM}$	Eddy diffusivity	1700	$\text{m}^2 \text{s}^{-1}$
$f_S$	Coriolis parameter	$-1 \times 10^{-4}$	$\text{s}^{-1}$
$\rho_0$	Reference density	1027.5	$\text{kg m}^{-3}$
$\kappa$	Vertical diffusivity	$1 \times 10^{-5}$	$\text{m}^2 \text{s}^{-1}$
$S_0$	Reference salinity	35	g/kg
$T_0$	Reference temperature	5	$^{\circ}\text{C}$
$T_{n,base}$	Base temperature box n	5	$^{\circ}\text{C}$
$T_{ts,base}$	Base temperature box ts	10	$^{\circ}\text{C}$
$\eta$	Hydraulic constant	$3 \times 10^4$	$\text{m s}^{-1}$
$\alpha$	Thermal expansion coefficient	$2 \times 10^{-4}$	$\text{K}^{-1}$
$\beta$	Haline contraction coefficient	$8 \times 10^{-4}$	$(\text{g/kg})^{-1}$
$r_S$	Transport by the southern subtropical gyre	$10 \times 10^6$	$\text{m}^3 \text{s}^{-1}$
$r_N$	Transport by the northern subtropical gyre	$5 \times 10^6$	$\text{m}^3 \text{s}^{-1}$
$E_s$	Symmetric freshwater flux	$0.56 \times 10^6$	$\text{m}^3 \text{s}^{-1}$

**Table S4.** Symbol (column 1), description (column 2), value (column 3), and units (column 4) of the general parameters used in the ocean circulation model added or changed with respect to Cimatoribus et al. (2014)

Symbol	Description	Value	Units
$E_s$	Symmetric freshwater flux	$0.56 \times 10^6$	$\text{m}^3 \text{s}^{-1}$
$d_{fn}$	Floor depth Box n	300	m
$d_{ft}$	Floor depth Box t	variable ( $D$ )	m
$d_{fts}$	Floor depth Box ts	variable ( $D$ )	m
$d_{fs}$	Floor depth Box s	300	m
$d_{fd}$	Floor depth Box d	4000	m
$T_{t,base}$	Base temperature Box t	23.44	$^{\circ}\text{C}$
$T_{s,base}$	Base temperature Box s	0.93	$^{\circ}\text{C}$
$T_d$	Temperature Box d	1.8	$^{\circ}\text{C}$

**Table S5.** Symbol (column 1), description (column 2), value (column 3), and units (column 4) of the general parameters used in the carbon cycle model based on Boot et al. (2022).

Symbol	Description	Value	Units
$V_{at}$	Volume of the atmosphere	$1.76 \times 10^{20}$	$\text{m}^3$
$F_{Ca,base}$	Base rain ratio	0.07	-
$n$	Order of $\text{CaCO}_3$ dissolution kinetics	1	-
$P_C$	Mass percentage of C in $\text{CaCO}_3$	0.12	-
$D_{Ca}$	Constant dissolution rate of $\text{CaCO}_3$	$2.75 \times 10^{-13}$	$\text{mol m}^{-3} \text{s}^{-1}$
$W_{SC}$	Constant silicate weathering	$2.4 \times 10^{-12}$	$\text{mol m}^{-3} \text{s}^{-1}$
$W_{SV}$	Variable silicate weathering parameter	$1.6 \times 10^{-8}$	$\text{mol m}^{-3} \text{atm}^{-1} \text{s}^{-1}$
$W_{CV}$	Variable carbonate weathering parameter	$6.3 \times 10^{-8}$	$\text{mol m}^{-3} \text{atm}^{-1} \text{s}^{-1}$
$k_{Ca}$	Constant $\text{CaCO}_3$ dissolution rate	$4.4 \times 10^{-6}$	$\text{s}^{-1}$
$b$	Exponent in Martin's law	0.75	-
$d_0$	Reference depth for biological productivity	100	m
$k_{w,base}$	Base piston velocity	3	m/day
$R_{C:P}$	Redfield C:P ratio	130	mol C/mol P
$R_{P:C}$	Redfield P:C ratio	1/130	mol P/mol C
$[Ca]_n$	Calcium concentration Box n	$0.01028 \times S_n$	$\text{mol m}^{-3}$
$[Ca]_t$	Calcium concentration Box t	$0.01028 \times S_t$	$\text{mol m}^{-3}$
$[Ca]_{ts}$	Calcium concentration Box ts	$0.01028 \times S_{ts}$	$\text{mol m}^{-3}$
$[Ca]_s$	Calcium concentration Box s	$0.01028 \times S_s$	$\text{mol m}^{-3}$
$[Ca]_d$	Calcium concentration Box d	$0.01028 \times S_d$	$\text{mol m}^{-3}$

**Table S6.** Symbol (column 1), description (column 2), value (column 3), and units (column 4) of the parameters used in the carbon cycle model that have been changed compared to Boot et al. (2022).

Symbol	Description	Value	Units
$Z_{n,base}$	Base biological production Box n	1.9	$\text{mol C m}^{-2} \text{yr}^{-1}$
$Z_{t,base}$	Base biological production Box t	2.1	$\text{mol C m}^{-2} \text{yr}^{-1}$
$Z_{ts,base}$	Base biological production Box ts	2.1	$\text{mol C m}^{-2} \text{yr}^{-1}$
$Z_{s,base}$	Base biological production Box s	1.1	$\text{mol C m}^{-2} \text{yr}^{-1}$
$\epsilon_{n,base}$	Base biological efficiency Box n	0.1	-
$\epsilon_{t,base}$	Base biological efficiency Box t	0.5	-
$\epsilon_{ts,base}$	Base biological efficiency Box ts	0.3	-
$\epsilon_{s,base}$	Base biological efficiency Box s	0.1	-
$R_{PO4}$	River influx of $\text{PO}_4^{3-}$	$0.3 \times 10^4$	

**Table S7.** The symbols and description of the equilibrium constants are presented in the first two columns. The third column presents the source of the used expression.

Symbol	Description	Expression
$K_0$	Solubility constant	Weiss (1974)
$K_1$	First dissociation constant of carbonic acid	Lueker, Dickson, and Keeling (2000)
$K_2$	Second dissociation constant of carbonic acid	Lueker et al. (2000)
$K_{sp,base}$	Equilibrium constant for $\text{CaCO}_3$ dissolution	Mucci (1983)
$K_{sp,press}$	Pressure correction for $K_{sp,base}$	Millero (1983)

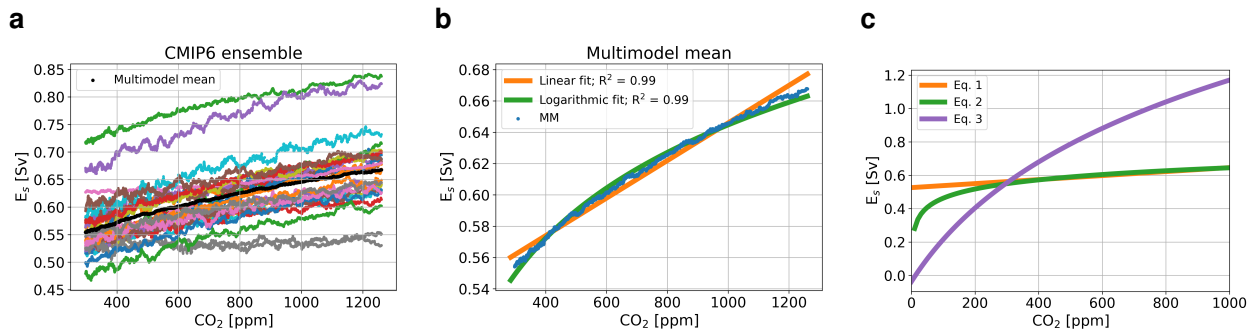


**Figure S1.** Symmetrical surface freshwater flux in Sv fitted to atmospheric  $\text{pCO}_2$  in a CMIP6 ensemble of 28 models. In panel a the colored lines represent CMIP6 models and the black line represents the multi-model mean. In panel b the multi-model mean (blue) and linear (orange) and logarithmic (green) fits are shown including the  $R^2$  values in the legend. In panel c the used fits used in the main text are displayed. The orange and green lines are similar to the ones in panel b. Orange represents Eq. 1, green Eq. 2, purple Eq. 3 (equations from main text).

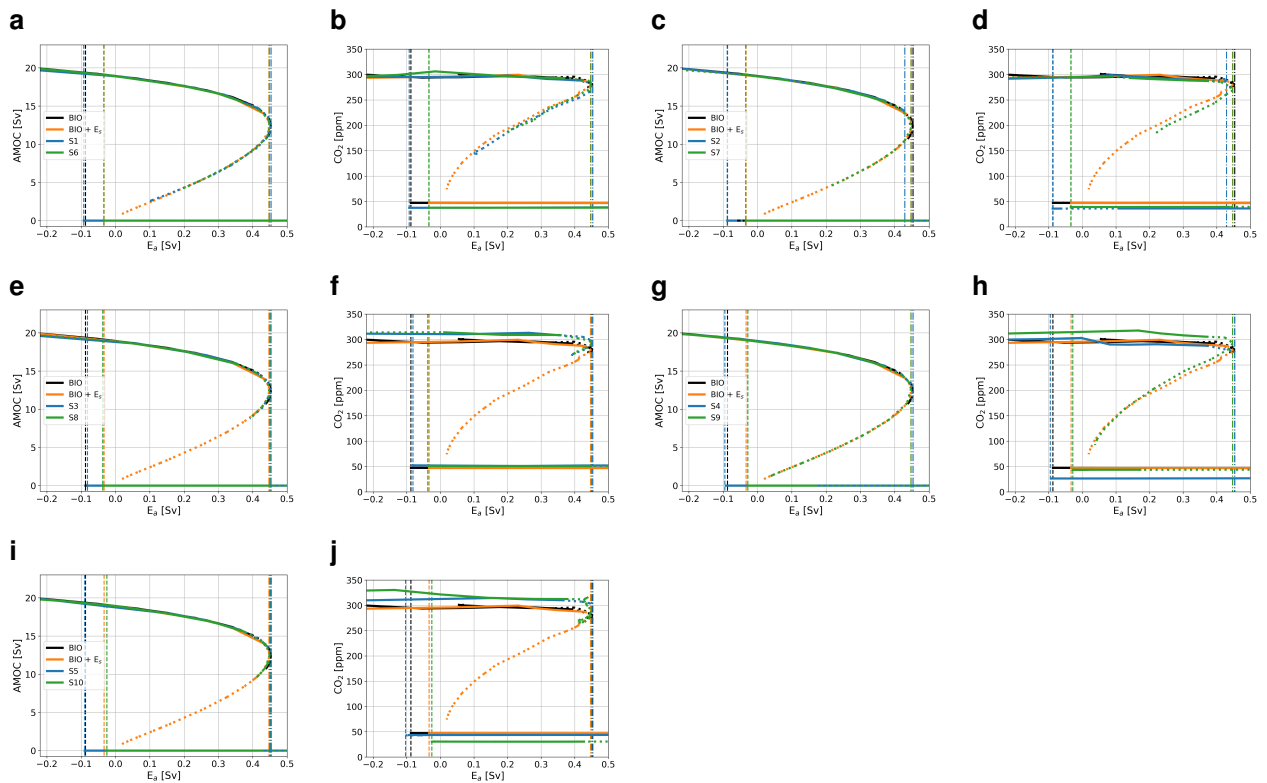


**Figure S2.** Bifurcation diagrams showing the sensitivity of the model to  $E_a$  for additional cases as defined in Table S2. Solid lines represent stable steady state solutions, dotted lines represent unstable states, dash-dotted lines represent the location of the saddle node on the on-branch, and dashed lines the location of the saddle node on the off-branch. The black lines represent a case with only the biological coupling (BIO), the orange lines with the logarithmic CMIP6 based  $E_s$  and biological coupling ( $E_s + \text{BIO}$ ), and the blue and green lines represent the cases defined in Table S2. Results are for the AMOC strength in Sv (a, c, e, g, i) and atmospheric  $p\text{CO}_2$  in ppm (b, d, f, h, j).

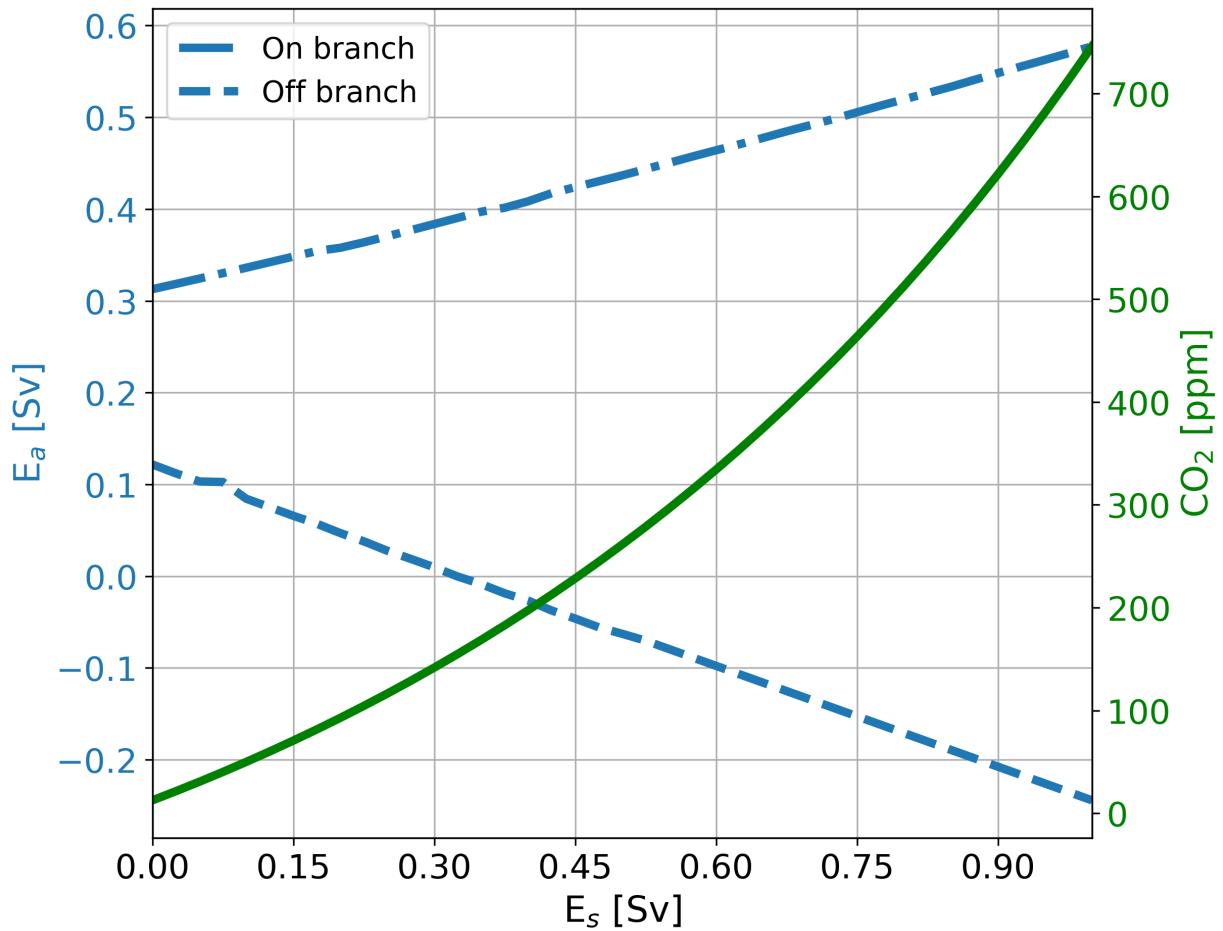


**Figure S3.** Sensitivity of the location in  $E_a$  of the saddle nodes in the circulation model to different values of  $E_s$ . The blue dashed dotted line represents the saddle node on the on-branch, and the blue dashed line the saddle node on the off branch. The green line, corresponding to the right y-axis, represents  $CO_2$  concentrations in ppm corresponding to the strong  $E_s$ - $pCO_2$ -coupling from the main text (Eq. 3) for the  $E_s$  values on the x-axis.